5.4 Intelligent Gravimetric Analysis of $NaNH_2BH_3$ and Aged $NaNH_2BH_3$

The decomposition reactions of $NaNH_2BH_3$ and aged-$NaNH_2BH_3$ were studied using intelligent gravimetric analysis combined with mass spectrometry (IGA-MS, Section 2.3.1). The samples were ground and loaded, under inert conditions, into the IGA-MS apparatus as outlined in Section 2.3.1. The sample was heated at 2°C min^{-1} under 1 bar of flowing He (100ml min^{-1}) to 250 °C (673K), and held there for 12 hours. A small aliquot of the outgoing gases were diverted to the dynamic sampling mass spectrometer, which was set to scan for materials of 2, 14, 17, 28 and 81 atomic mass units (AMU), corresponding to , H_2, NH_3, B_2H_6, $B_3N_3H_6$, respectively. Measurements of the sample mass (mg), temperature (°C), pressure (mbar), and the partial pressures of the released gases (μTorr) were taken every 0.2 minutes.

5.4.1 Intelligent Gravimetric Analysis Studies of $NaNH_2BH_3$

A total mass loss of 7.4% over two events was observed during the decomposition of the $NaNH_2BH_3$ sample (Figure 5.7) . The first mass loss of 5.9 % was observed as the temperature of the sample increased from 71°C - 112°C (344K - 385 K) and the second mass loss of 1.5 % occurred between temperatures of 116°C - 246°C (389K - 519 K). Differentiation of the mass loss with respect to temperature (see Figure 5.7 inset) confirmed these findings and revealed peak mass loses of the two events to be at 78°C (351K) and 167°C (440K).

The partial pressures of H_2 NH_3, B_2H_6, $B_3N_3H_6$ (2, 17, 28 and 81 AMU respectively) recorded by in-situ mass spectrometry, are presented in Figure 5.8. As can be seen from the data H_2 is the major decomposition product. No $B_3N_3H_6$ was observed at any point and only trace amounts of NH_3 and B_2H_6 ($7x10^{-4}$ and $1.1x10^{-4}$ μTorr) were observed during the first rapid mass loss event see Figure 5.7 inset. The lack of NH_3 evolution is in contrast to the findings of Fijakowski *et. al.* [96] who observed that 1 mole of NH_3 was released for every 10 moles of H_2. This is most likely to result from the different synthetic methods used. Fijakowski's sample was ball milled which nanostructures and can dope the sample with elements from the balls and milling jar [206]. Milling is

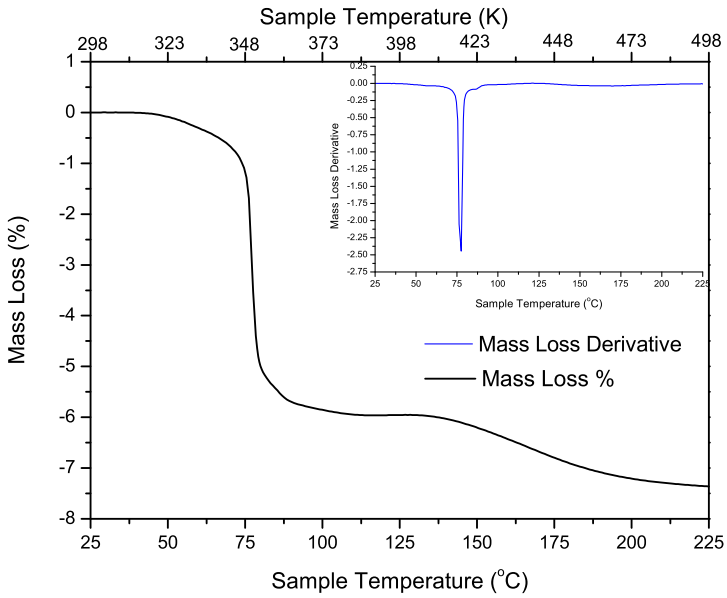

Figure 5.7: Thermogravimetric data of the decomposition of $NaNH_2BH_3$ collected using intelligent gravimetric analysis, with heating rate 2°C min^{-1} and target temperature of 250 °C. The black line represents the sample mass loss in %. Insert: differential of sample mass loss % with respect to temperature.

widely used to alter the decomposition [12] or other properties of a material [207, 61]. In their case, it is difficult to distinguish the inherent properties of the sample from any additional properties caused by milling.

X-ray diffraction studies of the decomposed sample showed that it contained predominantly NaH with trace amounts of $NaBH_4$ and hexagonal BN.

The combination of the above data provides evidence for the following two stage decomposition pathway:

$$n\mathrm{NaNH_2BH_3} \rightarrow \tfrac{3}{2}nH_2 + n\mathrm{NaH} + (\mathrm{NBH})_n$$

$$(\mathrm{NBH})_n \rightarrow \tfrac{1}{2}nH_2 + (\mathrm{NB})_n$$

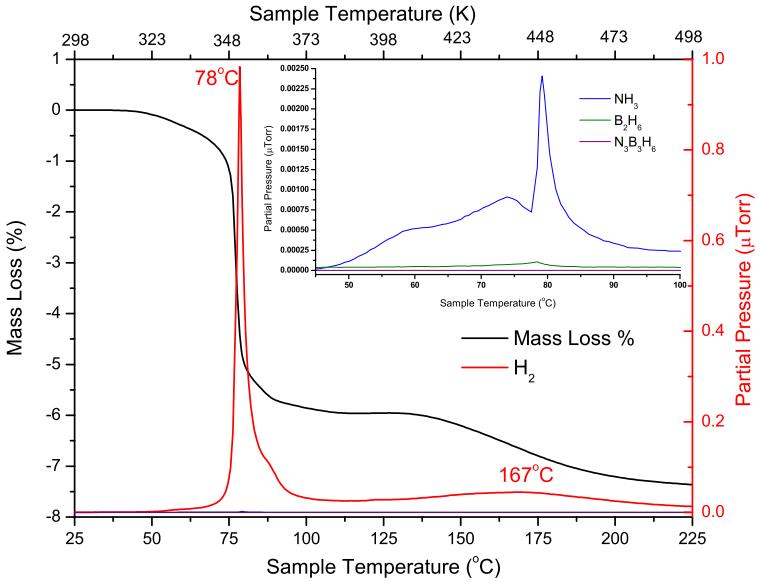

Figure 5.8: Thermogravimetric data of the decomposition of $NaNH_2BH_3$ collected using intelligent gravimetric analysis, with heating rate 2°C min^{-1} and target temperature of 250 °C (523K)(black line) and the partial pressures of H_2 (red line), recorded using in-situ mass spectrometry. Inset: partial pressures of NH_3 (blue line), B_2H_6 (green line), and $N_3B_3H_6$ (purple line) recorded using in-situ mass spectrometry are also presented.

The lower decomposition temperature of $NaNH_2BH_3$ (78°C or 351K) compared with $LiNH_2BH_3$ (92°C /365K) is to be expected as the larger Na^+ expands the crystal lattice and weakens the intermolecular interactions. The formation of significant amounts of NaH but no LiH can be rationalised for electronic and steric reasons. Firstly NaH is a more stable compound than LiH making it more likely that when a hydride is transferred to the metal ion during the decomposition it acts as a 'sink' rather than a transition state. Secondly, the larger size of the Na^+ means it may be too sterically hindered to stay attached to the polymeric N-B species formed.

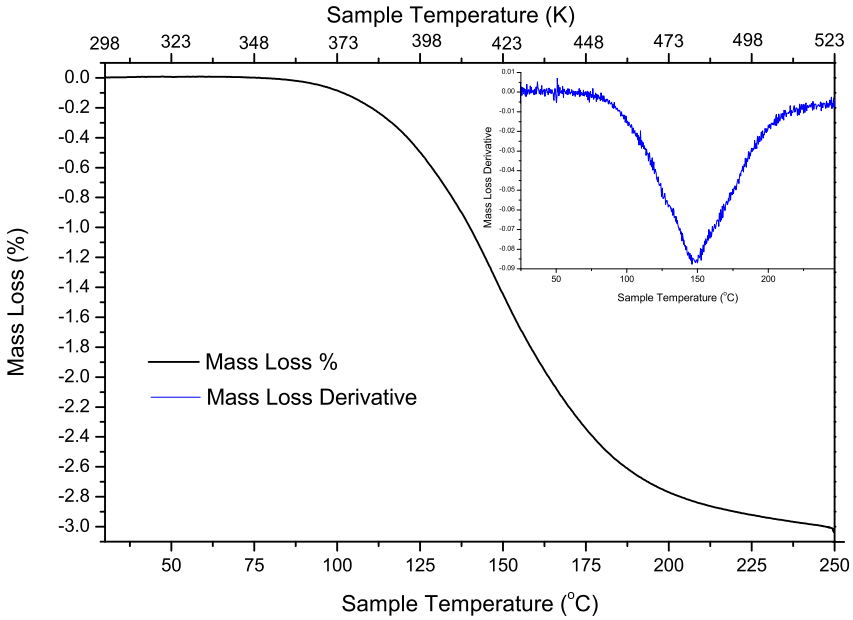

Figure 5.9: Thermogravimetric data of the decomposition of aged $NaNH_2BH_3$ collected using intelligent gravimetric analysis, with heating rate 2°C min^{-1} and target temperature of 250 °C (523K). The black line represents the sample mass loss in %. Insert: differential of sample mass loss % with respect to time

5.4.2 Intelligent Gravimetric Analysis Studies of aged $NaNH_2BH_3$

The thermogravimetric data for the decomposition of aged $NaNH_2BH_3$ are presented in Figure 5.9. A total mass loss of 2.5% over one event was observed during the decomposition of the aged $NaNH_2BH_3$ sample. The mass loss of 2.5% was observed over a very wide temperature range as the temperature of the sample increased from 87°C to 274°C(372 to 547 K). Differentiation of the mass loss with respect to temperature (see Figure 5.9 inset) confirmed these findings and revealed the peak mass loss of the event to be at 149°C (422K).

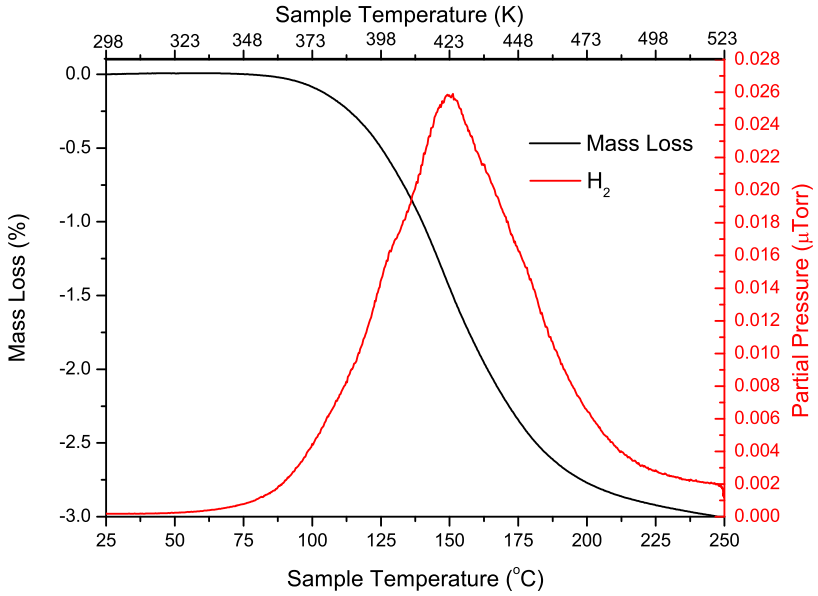

Figure 5.10: Thermogravimetric data of the decomposition of $NaNH_2BH_3$ collected using intelligent gravimetric analysis, with heating rate 2°C min^{-1} and target temperature of 250 °C (523K)(black line) and the partial pressures of H_2 (red line), recorded using in-situ mass spectrometry.

Mass spectrometry data, showing the partial pressure of H_2 (2 AMU) evolved from the sample as a function of time, are presented in Figure 5.10, with the thermogravimetric data added to aid comparison. All of the other gases sampled for (NH_3, B_2H_6, $B_3N_3H_6$ 17, 28 and 81 AMU respectively) were only present in negligible amounts. It is clear from this data that the observed mass loss is primarily due to the production of H_2. The peak evolution of H_2 agrees well with the peaks observed in the mass loss differentiation, with the peak H_2 evolution also being at 149°C.

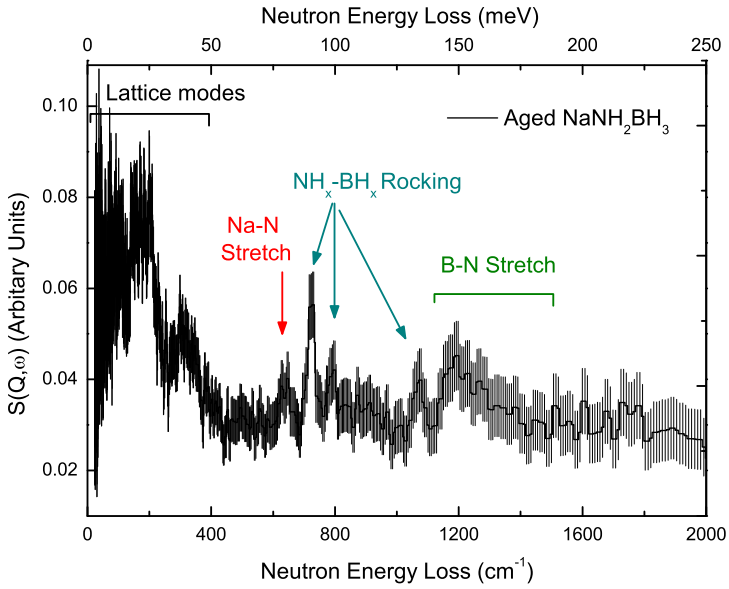

Figure 5.11: Experimental INS spectrum of aged $NaNH_2BH_3$ in the 0-2000 cm^{-1} region.

5.5 Inelastic Neutron Scattering Studies of Aged $NaNH_2BH_3$

The inelastic neutron scattering data for $NaNH_2BH_3$ were collected before the aging problem became apparent and unfortunately an older stock sample was used for the experiment. As a consequence there is no known structure to compute the phonon density of states and their the modes cannot be exactly assigned. Furthermore the poor crystallinity coupled with the nature of the sample resulted in ill defined peaks. However, using data from the $LiNH_2BH_3$ phonon density of states, it has been possible to assign regions of the spectrum presented in Figure 5.11.

The aged $NaNH_2BH_3$ spectrum can also be compared to the tetragonal lithium amidoborane spectrum Figure 5.12. Modes associated with Na rather than the Li are shifted to higher frequencies eg Na-N and LiN stretches and some of the lattice vibration modes, as it take more energy to move the heavier atom. Nevertheless, despite the shifts regions of the spectra have very similar shapes which suggests that $NaNH_2BH_3$ appears to age to an amorphous but analogous compound in terms of the molecular structure to the lithiated tetragonal phase.

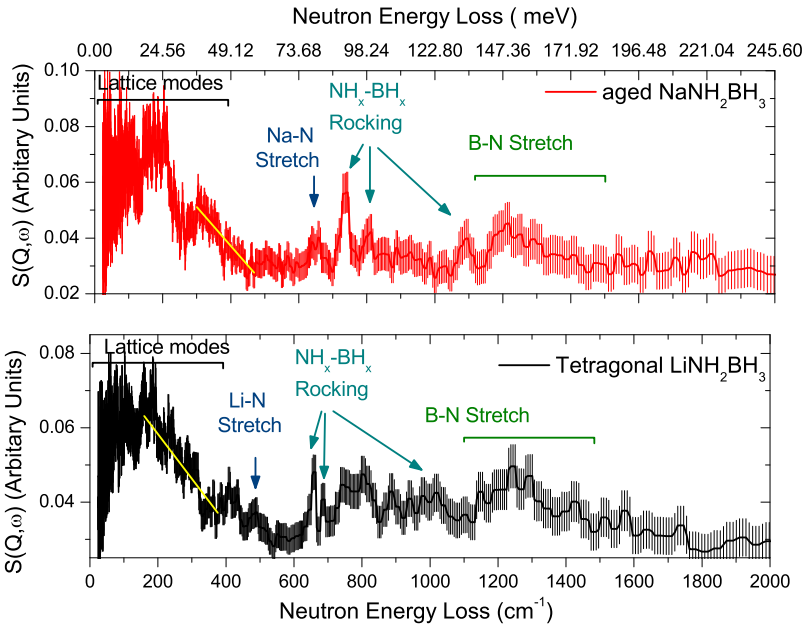

Figure 5.12: Comparison of experimental INS spectra: aged $NaNH_2BH_3$ (red) and Tetragonal-$LiNH_2BH_3$ (black) in the 0-2000 cm^{-1} region.

Common regions of the spectra include:

- A linear region in the lattice vibrations (yellow lines on Figure 5.12) centered at approx approx 300cm^{-1} on the Na spectrum and 250^{-1} on the Li spectrum. As previously discussed in Section 3.2.2, linear regions are often associated with rotation and disorder in a compound, consistent with the highly disordered structure of the lithiated tetragonal phase and the amorphous nature of the aged $NaNH_2BH_3$.
- Two sharp peaks in the NH_xBH_x rocking region which indicated a similar B-N structure

5.6 Conclusions

$NaNH_2BH_3$ was synthesised in a one pot room temperature reaction between NaH and NH_3BH_3 in diethyl ether. The structure of $NaNH_2BH_3$ was investigated by neutron powder diffraction and synchrotron X-ray powder diffraction. $NaNH_2BH_3$ was identified to have the space group *Pbca* and room temperature lattice constants of $a = 14.6474(32)$Å $b = 5.6548(09)$Å $c = 7.4680(16)$Å.

A variable temperature synchrotron X-ray diffraction study of $NaNH_2BH_3$ was also completed. The lattice parameters of $NaNH_2BH_3$ increased linearly with increasing temperature from 200K-345K (-73°C to 72°C) where upon they began to deviate from the fit with a complete loss of crystallinity at 351K (78°C). The anomalous behaviour prior to decomposition is related to highly anisotropic Na motion along the c axis at high temperatures.

A thermogravimetric analysis with mass spectrometry study of $NaNH_2BH_3$ was performed. $NaNH_2BH_3$ was heated to to 250°C (673K) under 1 bar of flowing He (100ml min^{-1}). The sample lost 7.4% of its weight over two decomposition events. The events had maxima at 78°C (351K) and 167°C (440K) respectively. The first maximum agrees well with the loss of crystallinity observed in the variable temperature synchrotron X-ray diffraction study. The mass spectrometer detected hydrogen as the major decomosition product along with trace amounts of diborane and ammonia.

$NaNH_2BH_3$ was found to be highly susceptible to degradation by radiation which decomposes it to NaH and an amorphous compound. $NaNH_2BH_3$ also ages transforming to an amorphous compound over a period of weeks.

The aged $NaNH_2BH_3$ compound was studied by thermogravimetric analysis with mass spectrometry under the same conditions as $NaNH_2BH_3$. The aged sample lost 2.5% over a broad decomposition step. The peak mass loss of the event was at 149°C (422K) with hydrogen as the only decomposition product.

The INS spectrum of aged $NaNH_2BH_3$ was also collected. Complete assignment of the modes was not possible due to the lack of a crystal / molecular structure. General regions of the spectra could however be identified. Parallels were drawn between the aged $NaNH_2BH_3$ and the lithiated tetragonal phase.

Chapter 6

Potassium Amidoborane

6.1 Introduction And Chapter Outline

KNH_2BH_3 is the the third alkali metal amidoborane to be synthesised and is currently the least studied of all the amidoborane complexes; to date only one paper has been published [89]. This chapter presents a synthetic, crystallographic and thermogravimetric study of KNH_2BH_3. Structural work was undertaken in conjunction with collaborators in Los Alamos National Laboratory (LANL). Single crystals of KNH_2BH_3 were grown at LANL and the structure determined by a single crystal X-ray diffraction study. Concurrently, high purity powder samples were prepared in Oxford as described earlier and used for the rest of the experimental described in this chapter.

The structure of KNH_2BH_3 was explored in detail with synchrotron X-ray powder diffraction at the SLS on the MS X04SA high-resolution beamline (Section 2.2.2) and neutron powder diffraction on HRPD at ISIS (Section 2.2.3). Variable temperature synchrotron X-ray powder diffraction measurements were also taken to monitor the changes in crystal structure up to decomposition.

Hydrogen desorption properties were studied first using combined intelligent gravimetric analysis with mass spectrometry (IGA-MS, Section 2.3.1) and then using the (IGA^n) apparatus (Section 2.3.1) in conjunction with the HRPD diffractometer.

6.2 Crystal structure of KNH_2BH_3

6.2.1 X-ray Diffraction of KNH_2BH_3

A sample of KNH_2BH_3 was synthesised via the reaction of KH with NH_3BH_3 in benzene at room temperature (Section 2.5.1). Diffraction data for the KNH_2BH_3 formed was collected at the SLS, on the MS X04SA high-resolution beamline, in a sealed capillary tube as described previously (Section 2.2.2) with X-ray radiation of wavelength of 0.800Å and a step-size of 0.004°.

The structure obtained from the single crystal data collected at Los Alamos was used as the starting point for the refinements. The data were analysed using the Rietveld method [129] and a rigid body analysis utilising TOPAS Academic fitting software [125] according to the general refinement procedure outlined in Section 2.2.4.

6.2.2 Neutron Diffraction of $KND_2{}^{11}BD_3$

A sample of $KND_2{}^{11}BD_3$ was synthesised via the reaction of KH with $ND_3{}^{11}BD_3$ in benzene at room temperature (section 2.6.1.1). Diffraction data for the KND_2BD_3 formed were collected on the HRPD beamline at ISIS in a 6mm vanadium can with an indium seal (Section 2.2.3).

The structure obtained from the SLS X-ray diffraction data was used as a starting point for the refinements. The data were analysed using the Rietveld method [129] and a rigid body analysis utilising TOPAS Academic fitting software [125] according to the general refinement procedure outlined in Section 2.2.4.

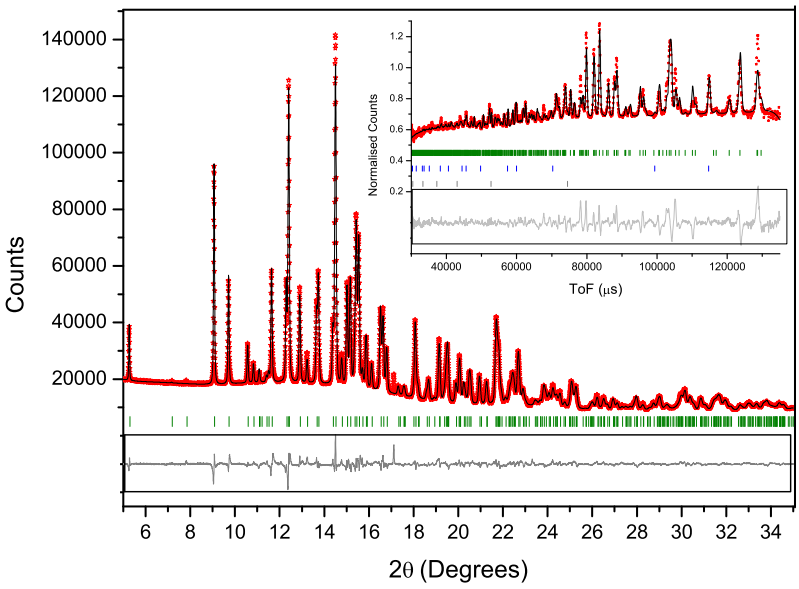

Figure 6.1: Final Rietveld refinement plots for X-ray and neutron (inset) diffraction data showing observed (black) , calculated (red) and difference (grey) plots. Bragg peak positions for the KNH_2BH_3 (green) are indicated.

All three detector banks were refined simultaneously. Incomplete deuteration was allowed for by mixed H/D site occupancy, allowing the D occupancy to refine between 0 and 1 while the total H and D occupancy was constrained to unity.

6.2.3 Simultaneous Rietveld Refinement of KNH_2BH_3

Finally, both the X-ray and Neutron data sets were refined simultaneously to achieve a unified structure (see Figure 6.1) and the refined structural parameters are shown below in Table 6.1.

KNH_2BH_3 is an ionic salt consisting of $[K]^+$ ions and $[NH_2BH_3]^-$ molecular anions in an orthorhombic unit cell with lattice constants a = 9.4304(1) Å, b = 8.2611(1) Å, and c = 17.3403(2)Å space group *Pbca*. The structure of KNH_2BH_3 (Figure 6.2a) differs substantially from the analogous compounds $LiNH_2BH_3$ and $NaNH_2BH_3$ (see Sections 4.2 and 5.2). While all three compounds share the same space group, in isostructural

Atom	x/a	y/b	z/c	Occupancy	B_{iso} / Å^2	Wyckoff Positions
K1	0.35507	0.13346	0.60886	1	4.231	8c
K2	0.23816	0.07811	0.32582	1	4.231	8c
N1	0.09468	0.31536	-0.02543	1	3.82	8c
N2	-0.08464	-0.01466	0.31798	1	3.82	8c
B1	0.18287	0.16131	-0.02662	1	2.09	8c
B2	-0.03965	-0.17452	0.28208	1	4.54	8c
H1	0.02445	0.32850	0.02485	1	1.84	8c
H2	0.01784	0.33372	-0.05496	1	1.84	8c
H3	0.27993	0.13370	-0.07162	1	1.84	8c
H4	0.23344	0.15775	0.04001	1	1.84	8c
H5	0.08350	0.08506	-0.03578	1	1.84	8c
H6	-0.06042	-0.06019	0.37297	1	1.84	8c
H7	-0.16891	-0.01154	0.31276	1	1.84	8c
H8	-0.09297	-0.17776	0.22116	1	1.84	8c
H9	0.08416	-0.16480	0.28152	1	1.84	8c
H10	-0.06401	-0.29115	0.31802	1	1.84	8c

Table 6.1: Atomic positions of KNH_2BH_3. $R_{wp} = 3.27$ $R_{exp} = 0.93$ χ^2 3.51

α-$LiNH_2BH_3$ and $NaNH_2BH_3$ the Li/Na^+ ions are tetrahedrally coordinated by a strong electrostatic interaction with the N^- at the apex and 3 weaker electrostatic interactions with the closest BH_3 units. In KNH_2BH_3 there are two distinct K, N and B atomic sites and each K^+ ion is octahedrally coordinated in *mer* symmetry by three $[NH_2BH_3]^-$ units and three BH_3 units, (as shown in Figure 6.2b) analogous to KBH_4 [208] and KNH_2 [205]. The higher coordination number confers greater stability on the larger, more diffuse, cation. Additionally, the *mer* symmetry is favorable as it allows the maximum separation between the three N coordinated amidoborane units.

The electrostatic interaction between the $[M]^+$ ions and $[NH_2BH_3]^-$ results in strong, directional M-N bonds. The K-N bond distances range between 3.02Å - 3.14 Å and are close to the K-N bond distance seen in KNH_2 (3.08 Å) [205]. They are more than 2.0Å longer than the H-N bond they replace in NH_3BH_3 and this substitution therefore

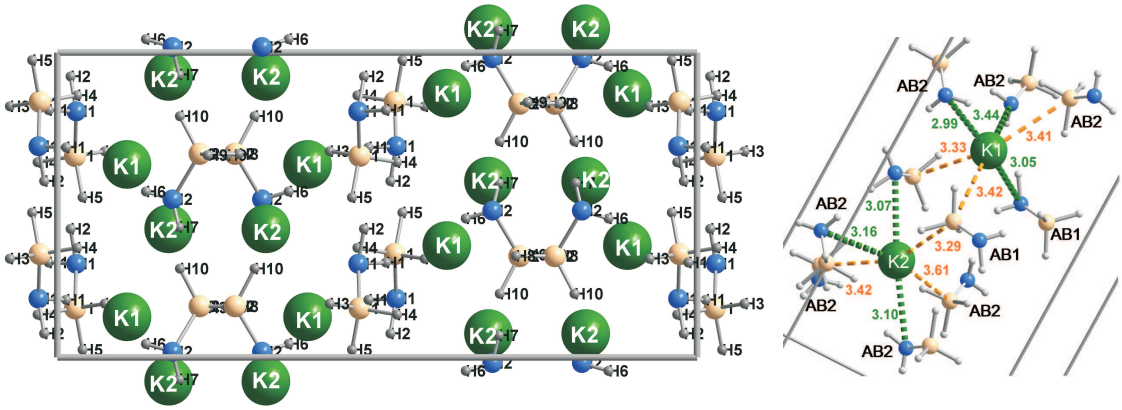

Figure 6.2: (a) *a*-axis projection of KNH_2BH_3 (b) the octahedral coordination of K^+ ions highlighting the short K-N bonds and K-BH_3 close contacts in Å. Potassium is green, nitrogen blue and boron cream.

results in an expansion of the unit cell and the disappearance of dihydrogen bonding. The closest intermolecular $H^{\delta+} \cdots H^{\delta-}$ distances increase from 1.96 Å(NH_3BH_3) to 2.27 Å (KNH_2BH_3), which are close to the expected van-der-Waals distances (2.4 Å), and thus likely to be very weak interactions. The $H^{\delta+} \cdots H^{\delta-}$ distance is shorter than the one observed in α-$LiNH_2BH_3$, and $NaNH_2BH_3$ (2.37Å and 2.72Å respectively) due to the change in coordination of the cation from tetrahedral to octahedral, thereby increasing the packing density of the $[NH_2BH_3]^-$ anions.

The next most significant interactions in the KNH_2BH_3 structure are the electrostatic interactions between K^+ and the three closest BH_3 units. The presence of these B-$H^{\delta-} \cdots M^+$ interactions supersede the dihydrogen bonding seen in NH_3BH_3 as the stabilizing factor of the extended structure. These are of sufficient energy so that the KNH_2BH_3 remains a solid at room temperature despite the absence of the dihydrogen bonding. The K-B distances of 3.32 Å, 3.38 Å and 3.61Å are similar to those seen in KBH_4 (3.36 Å) [205]. There are also a number of additional interactions between the cation and hydric hydrogens which further stabilize the larger more diffuse cation.

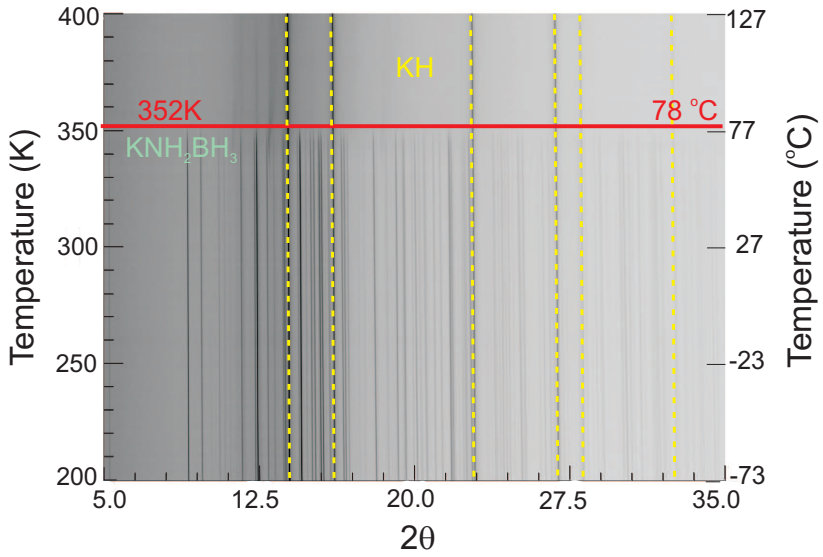

Figure 6.3: Surface plot of synchrotron X-ray diffraction data collected during the heating of KNH_2BH_3 400K (127°C) in a sealed glass capillary tube. Lines corresponding to Bragg reflections of KH are highlighted.

6.3 Variable Temperature X-ray Diffraction Studies of KNH_2BH_3

Variable temperature X-ray powder diffraction patterns of KNH_2BH_3 were collected between 200K-400K (-73°C- 127°C) in 1K steps on MS X04SA, the high-resolution beamline at the SLS (see Section 2.2.2). The data sets were refined sequentially in a batch file as detailed in Section 2.2.4.

Inspection of the Bragg peaks during variable temperature X-ray diffraction experiments revealed that they broadened and flattened with increasing temperature, with a complete disappearance of crystalline KNH_2BH_3 at 352K (79°C) (see Figure 6.3). After the disappearance of the KNH_2BH_3 peaks, the background of the patterns rose indicating an increase in the amount of amorphous material in the sample.

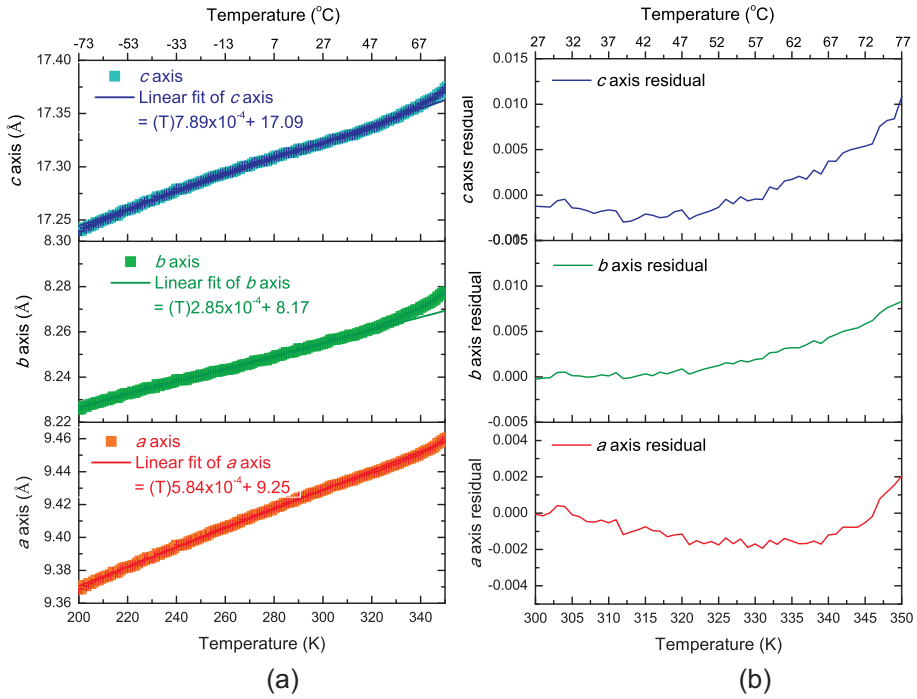

Figure 6.4: Graphs showing (a) refined KNH_2BH_3 lattice parameters, calculated from Rietveld analysis of synchrotron diffraction data (via batch refinement) collected during the heating of KNH_2BH_3 between 200-352K (-73-77°C) Linear fits of the relationship between temperature and the axis length are displayed on the graphs (b) Residual plots of the difference between the experimental lattice parameters and the fit between 300K-350K (27°C-77°C). Mean errors, $a \pm 0.00011$, $b \pm 0.00010$ $c \pm 0.00021$. Error bars only shown if larger than data markers.

The disappearance of crystalline KNH_2BH_3 at 352K (79°C) is slightly lower than the onset of decomposition observed by thermogravimetric measurements on this sample *ca.* 353K (80°C). This, and the increase in background in subsequent data sets, is consistent with KNH_2BH_3 transforming to an amorphous state just prior to decomposition. Initially it was thought that the sample melted but observations with a melting point apparatus (Section 2.4.2) proved this was not the case and the amorphous phase is solid.

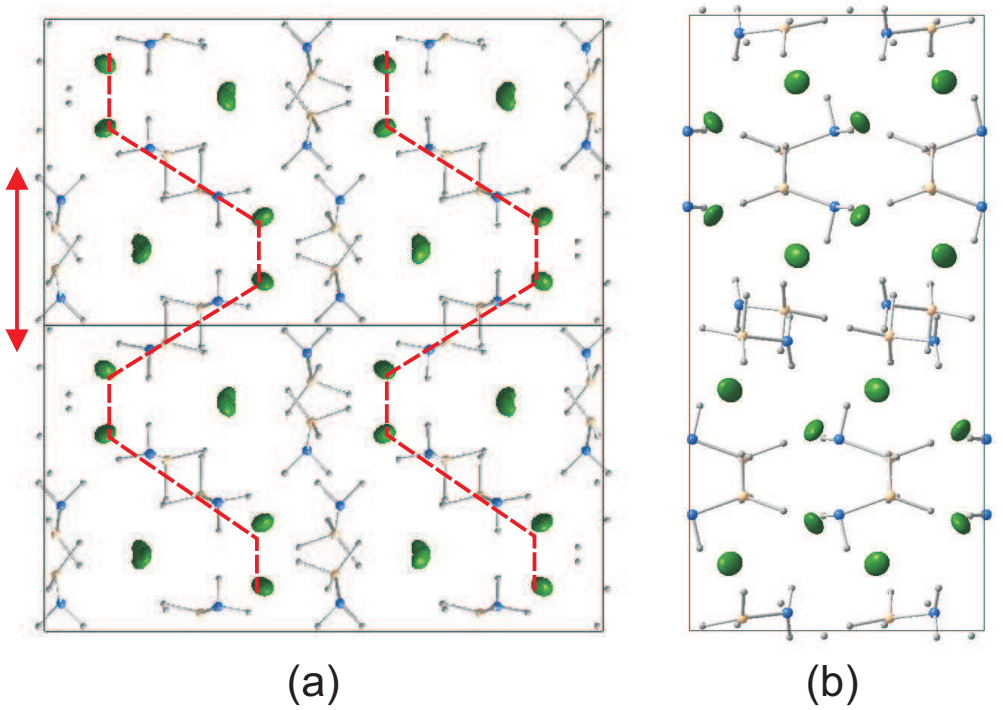

Figure 6.5: Structural diagrams of KNH_2BH_3 at 348K (75°C) showing refined ADPs for the K atoms (ellipsoid probabliity 1). Viewing directions along (a)the *a*-*c* plane and (b) the *b* axis. Potassium is green, nitrogen blue and boron cream.

All the KNH_2BH_3 lattice parameters were found to increase linearly with temperature, but with significant anisotropic expansion. The *a* axis expanded by +0.98% , the *b* axes by +0.63% and the *c* axis by +0.79%. Perhaps surprisingly it is not the long *c* axis that had the greatest expansion but the shorter *a* axis. However, if the unit cell is viewed along the *a*-*c* plane (Figure 6.5 a) 'zigzagging' chains of K atoms can be seen running parallel to the a axis. It is clear to see how there is a large potential for expansion if the zigzags widen, a fact confirmed by the crystallographic data. Comparison of the 200K and 348K (-73°C and 75°C) unit cells showed: The internal zig-zag angles widened from 70.39° to 70.52° and the closest K$\cdots$K distances increased from 4.22Å to 4.25Å.

Conversely, the axis which deviates the most from linear expansion above 315K (42°C) is the *b* axis, as shown by the residual plots in Figure 6.4(b). The *b* axis deviation begins at 315K (42°C) where as the significant deviation for the other axis does not commence until over 320K (47°C). Figure 6.5 also displays the refined ADPs for the K atoms at 348K (75°C) and from Figure 6.5 b it is clear that the motion is orthogonal. The largest ellipsoid parameter for the K1 sites is the U_{33} which means its motion is predominantly along the *c* axis but the largest ellipsoid parameter for the K2 sites is the U_{11} meaning motion is predominantly along the *a* axis. This juxtaposition of K atomic motion means the *b* axis is anticipated to be under a certain amount of stress and increases more quickly to maintain a reasonable separation between the K1 and K2 sites.

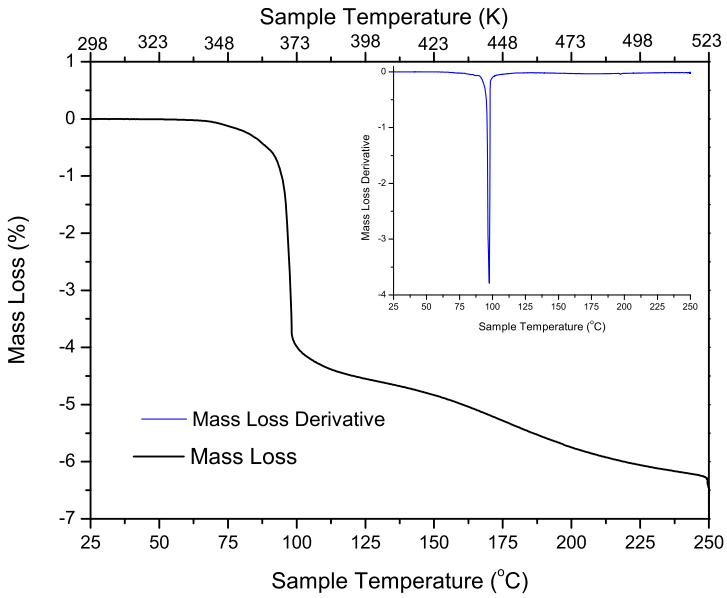

Figure 6.6: Thermogravimetric data of the decomposition of KNH_2BH_3 collected using intelligent gravimetric analysis, with heating rate 2°C min^{-1} and target temperature of 250°C (523K). The black line represents the sample mass loss in %. Inset: differential of sample mass loss % with respect to temperature.

6.3.1 Intelligent Gravimetric Analysis Studies of KNH_2BH_3

The thermogravimetric data for the decomposition of KNH_2BH_3, accompanied by its hydrogen desorption signal, are presented in Figure 6.6. A total mass loss of 5.8% over two events was observed during the decomposition of the KNH_2BH_3 sample. The first mass loss of 4.4% was observed as the temperature of the sample increased from 71°C to 112°C (344K to 385K) and the second mass loss of 1.4% occurred between temperatures of 123°C to 235°C (396K - 508 K). Differentiation of the mass loss with respect to time (see Figure 6.6inset) confirmed these findings and revealed peak mass loses of the two events to be at 98°C (371K) and 179°C (477K).

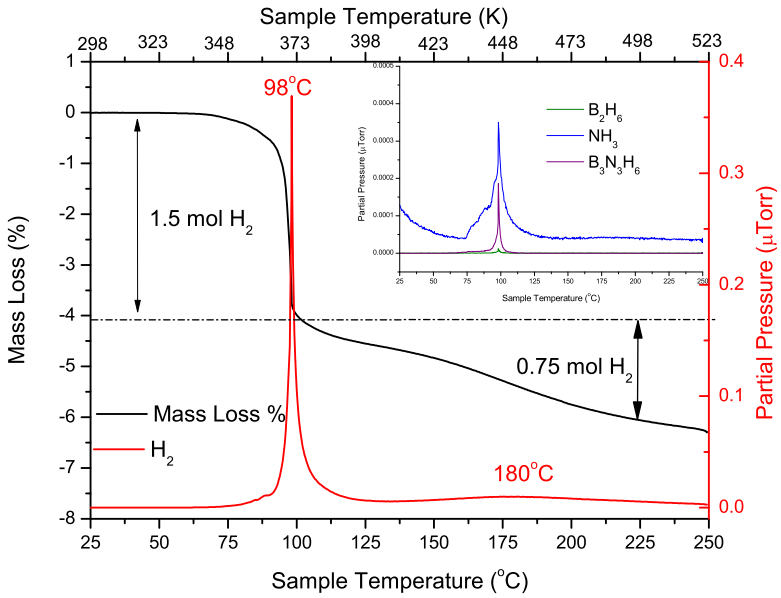

Figure 6.7: Thermogravimetric data of the decomposition of KNH_2BH_3 collected using intelligent gravimetric analysis, with heating rate 2°C min^{-1} and target temperature of 250°C (523K)(black line) and the partial pressures of H_2 (red line), recorded using in-situ mass spectrometry. Inset: partial pressures of NH_3 (blue line), B_2H_6 (green line), and $N_3B_3H_6$ (purple line) recorded using in-situ mass spectrometry are also presented.

The partial pressures of H_2, NH_3, B_2H_6 and $B_3N_3H_6$ (2, 17, 28 and 81 AMU respectively) recorded by in-situ mass spectrometry, are presented in Figure 6.7 b. As can be seen from the data, H_2 is the major decomposition product. Only trace amounts of NH_3, $B_3N_3H_6$ and B_2H_6 (3.5x10^{-4}, 1.9x10^{-4} and 1.2x10^{-5} μTorr) were observed during the first rapid mass loss event see Figure 6.7 inset. The peak H_2 evolution seen in the IGA begins 20 degrees higher than the decomposition seen in the variable temperature X-ray pattern which indicates the compound melts before it decomposes and the anomalous lattice expansion observed at 335K (62° C) is likely to be the onset of this event.

The decomposed residue contains significant amounts of KH and trace amounts of KBH_2 and BN. This combination of this data provides evidence for the following two step decomposition pathway:

$$n\mathrm{KNH_2BH_3} \rightarrow \tfrac{3}{2}n\mathrm{H_2} + \mathrm{KH} + (\mathrm{NBH})_n$$

$$(\mathrm{NBH})_n \rightarrow \tfrac{1}{2}n\mathrm{H_2} + (\mathrm{NB})_n$$

6.3.2 Intelligent Gravimetric Analysis with Neutron Diffraction Studies of $KND_2{}^{11}BD_3$

Intelligent gravimetric analysis combined with neutron diffraction (IGA^n) has been described in detail in Section 2.3.1. The following section presents the data gathered from the IGA^n study of $KND_2{}^{11}BD_3$, which was performed in order to gain a greater understanding of the crystallographic processes which occur during decomposition.

Synthesis, Primary Characterisation and Experiment Conditions

A sample of $KND_2{}^{11}BD_3$ was synthesised via the reaction of KH with $ND_3{}^{11}BD_3$ (Sections 2.5.1 and 2.5.2). The material was ground and loaded into a vanadium can under inert atmosphere and then transferred into the HRPD diffractometer (Section 2.2.3). Neutron diffraction data on this sample were collected at room temperature over a period of one hour in order to determine the composition of the $KND_2{}^{11}BD_3$ sample to be studied during the in situ diffraction experiments. Rietveld analysis [129] of the data using TOPAS Academic [125] (Section 2.2.4) indicated that the sample was majority phase $KND_2{}^{11}BD_3$ (89.6 %) with KD impurity (10.3%).

Having collected neutron diffraction data from the $KND_2{}^{11}BD_3$ sample at room temperature (Section 6.2.2), the sample was loaded into a vanadium bucket, which was in turn loaded into the IGA^n apparatus, as outlined in Section 2.3.1. The quartz reaction chamber was outgased to a pressure of 6 mbar and the sample was heated to 120 °C (393K) in 5 degree steps. Each temperature was held for 45 min before moving onto the next temperature. Neutron diffraction data were collected at intervals of 15 minutes throughout the course of the experiments, and thermogravimetric data were recorded approximately every 15 seconds.

Decomposition of the $KND_2{}^{11}BD_3$ Sample

A surface plot of the diffraction data collected, displayed in tandem with the corresponding thermogravimetric data, is shown in Figure 6.8. The intensity of the Bragg reflections is indicated by the colour of the lines, ranging from dark blue (background intensity) through pale blue (low intensity) and yellow (medium intensity) up to red (high intensity).

The Bragg reflections were indexed to $KND_2{}^{11}BD_3$, KH, Vanadium from the sample bucket and steel from the thermocouple. A d-spacing range of 2.2Å - 3.9Å is presented as this range includes a number of reflections of $KND_2{}^{11}BD_3$, the <111> reflection of KH and the <111> reflection of the steel, but excludes reflections arising from diffraction by the vanadium sample bucket.

The positions of the Bragg reflections for each phase present appeared to vary linearly with temperature, which is consistent with positive thermal expansion. The intensity of the $KND_2{}^{11}BD_3$ Bragg reflections began to decrease as the temperature of the sample reached 80°C (353K, run number 28), and had disappeared completely by the time the sample reached 85°C (358K, run number 31).

Study of the corresponding thermogravimetric data shows that the mass of the sample started to decrease immediately upon heating, which presumably arose because of the desorption of physisorbed gas from powder grains. The slight step at 115 mins is due to the IGA^n run being aborted and then restarted because of a period of beam loss. This slow mass loss began to gain momentum as the sample reached 55°C and then decreased sharply by 3.4% between 60-75°C (333-348K). The mass loss then slowed over the remainder of the experiment eventually reaching a total of 7.2% mass loss.

Analysis of the gravimetric data is made more complex because of the incomplete deuteration of the $KND_2{}^{11}BD_3$ sample. Rietveld refinement of the sample allowing fractional D and H occupancies on the same site revealed an D:H ratio of 1:0.17 and the effective RMM of 73.7 AMU not the theoretical 75 AMU of a fully deuterated sample. Of the 7.2% mass lost over the duration of the experiment 0.3% was thought to be due to the desorption of physisorbed gas from powder grains and the remaining 6.9% was assigned to the $KND_2{}^{11}BD_3$ decomposition. A mass loss of 6.9% from 73.7 AMU corresponds to a loss of 5.1 AMU or 2.9 D/H atoms:

$$n\mathrm{KN(D/H)_2{}^{11}B(D/H)_3} \rightarrow \tfrac{3}{2}n\mathrm{(D/H)_2} + (\mathrm{KN(D/H)^{11}B(D/H)})_n$$

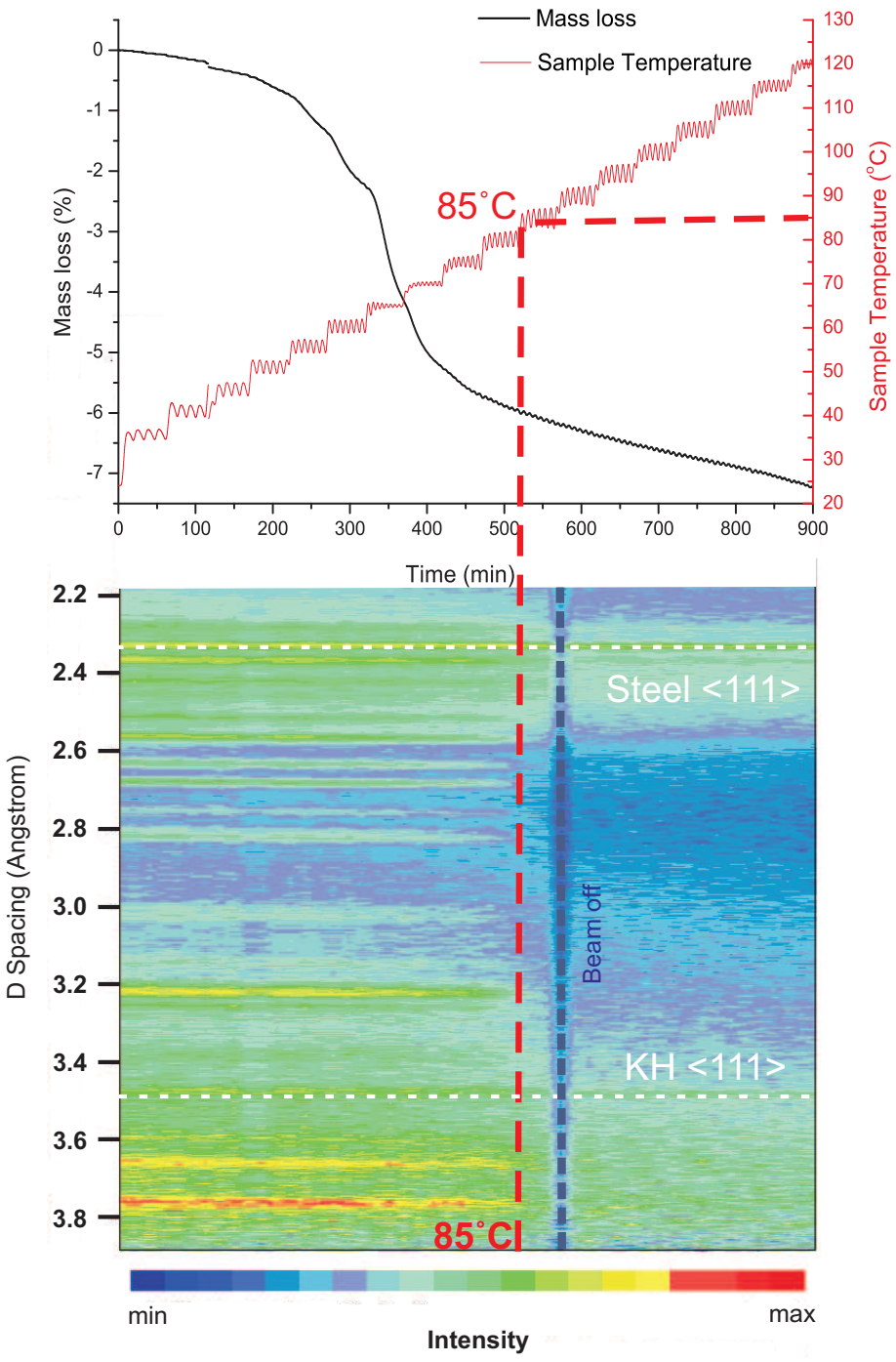

Figure 6.8: Comparison of the surface plot of neutron diffraction data (collected at bank 2) and thermogravimetric data collected during the decomposition of $KND_2{}^{11}BD_3$ in the IGA^n apparatus at constant pressure (6 mbar). d-spacing region of 2.3 - 2.7 Å. Ripples in the temperature are because of the feedback mechanism employed by the furnace to maintain a constant temperature.

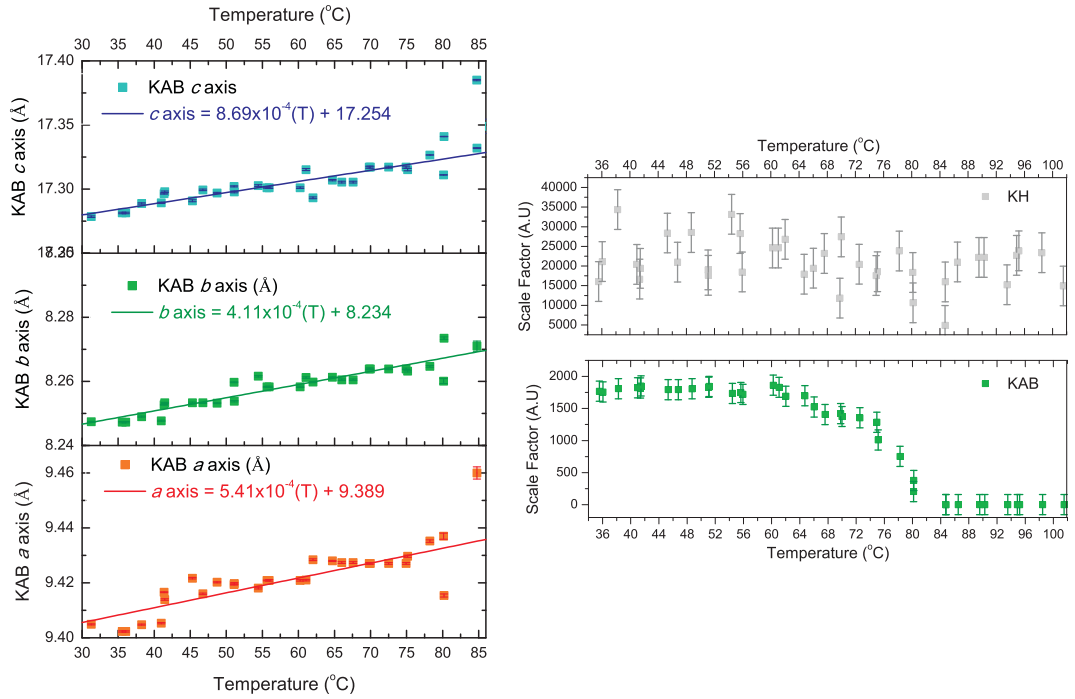

Figure 6.9: Summary of refined lattice parameters and scale factors, obtained from Rietveld analysis (via batch refinement) of the neutron diffraction data collected during the decomposition of $KND_2{}^{11}BD_3$ in the IGA^n.

Whilst the surface plot gives a qualitative overview of the IGA^n experiment, a quantitative understanding of the processes occurring can only be obtained through full Rietveld analysis [129] of each diffraction pattern. This analysis was performed using the batch facility of the TOPAS Academic software suite [125] following the general procedure outlined in Section 2.2.4.

The refined lattice parameters of $KND_2{}^{11}BD_3$ and the refined scale factors of $KND_2{}^{11}BD_3$ and KH are displayed in Figure 6.9.

The lattice parameters of $KND_2{}^{11}BD_3$ were all observed to vary linearly with the temperature of the sample up to the loss of crystallinity and decomposition of the sample at 86°C (359K). The expansion is anisoptropic, as previously observed from the variable temperature X-ray diffraction studies described in Section 6.3, but to a much lesser extent. In this case the there was only a 0.06% range a axis expanded the most (+0.32%), the c axis next by +0.28% and the b axis by +0.26%, where as for the variable temperature X-ray diffraction studies the range was 0.35%

Figure 6.9 shows that the plot for the $KND_2{}^{11}BD_3$ scale factors follows the same trend as that observed for the sample mass. Whereas the plot for the KH scale factors remains essentially constant throughout the experiment.

6.3.3 Differential Scanning Calorimetry of KNH_2BH_3

The experimental details of the DSC data collected in this thesis are described in Section 2.3.2 and the data are presented in Figure 6.10. Unlike $LiNH_2BH_3$ (Section 4.4.2) the KNH_2BH_3 trace bears no resemblance to the IGA data(Section 6.3.1). Instead the trace shows a substantial endotherm, immediately followed by an exotherm, which was also observed by Diyabalanage *et al.* [89].

The endotherm, between 50°C -69°C (323-342K), is sharp and has its maximum at 67°C (340K). Diyabalanage *et al.* [89] attributed this to a melt transition but analysis with melting point apparatus did not reveal a liquid phase. An alternative explanation is the re-orientation of the crystal phase into an amorphous solid phase [209]. The octahedral coordination in crystalline KNH_2BH_3 is rigid and does not allow the crystal much flexibility on heating. As the temperature increases, the crystallite become more strained and while the temperature is too low to decompose the structure completely, the extra energy can be used to 'relax' the structure into an amorphous state. Integration of the area under the peak with respect to time allowed the molar enthalpy change to be calculated. The calculated value for the crystalline amorphous phase transition was $\Delta H = +4.16$ kJ mol^{-1}.

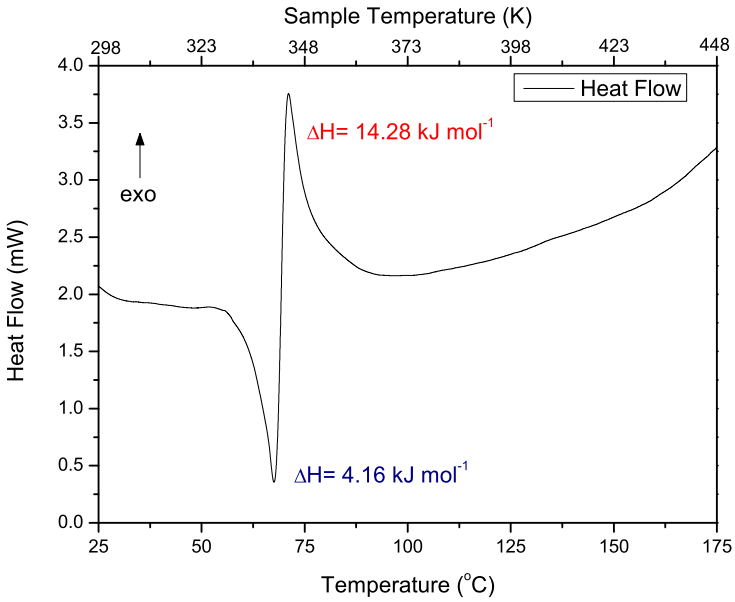

Figure 6.10: DSC trace of the decomposition of KNH_2BH_3 heated to 175°C (448K) at 1°C min^{-1}.

The exothermic peak is even shaper, occurring between 70°C - 97°C (343K-370K) with a maximum at 71°C (340K). This corresponds to the first stage of H_2 desorption;

$$n\mathrm{KNH_2BH_3} \rightarrow \tfrac{3}{2}n\mathrm{H_2} + n\mathrm{KH} + (\mathrm{NBH})_n$$

The calculated enthalpy change is ΔH = -14.29 kJ mol^{-1}. Still less exothermic than the NH_3BH_3 value of about -20 kJ mol^{-1} [193] but nearly three times greater then that calculated for $LiNH_2BH_3$ -4.99 kJ mol^{-1}

Above 97°C (370K), there is a steady increase in heat flux to the sample, that is indicative of a prolonged slow exothermic process from the polymeric B-N intermediate.

$$(\mathrm{NBH})_n \rightarrow \tfrac{1}{2}n\mathrm{H_2} + (\mathrm{NB})_n$$

The prolonged nature of the release suggests that $(NBH)_n$ is more stable than its lithiated analog described in Section 4.4.2

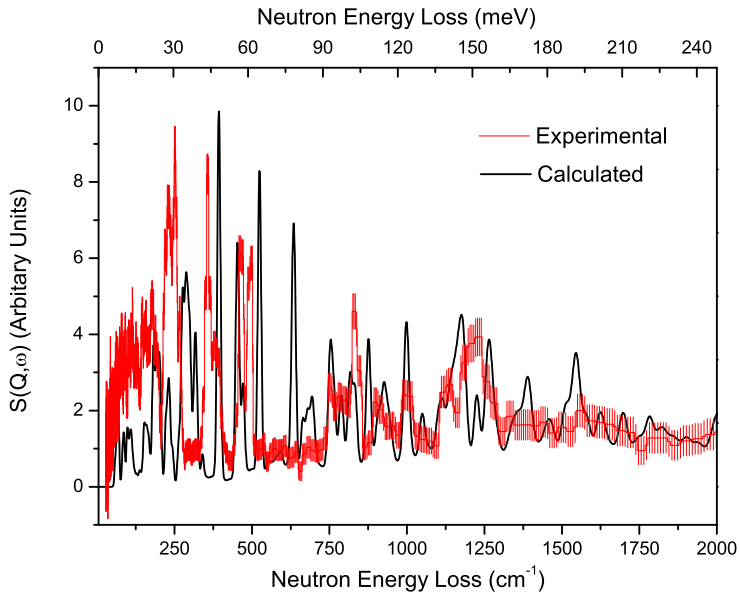

Figure 6.11: Comparison of INS spectra: experimental (red) and calculated by CASTEP for the complete unit cell (black) in the 0-2500 cm^{-1} region.

6.4 Inelastic Neutron Scattering Studies of KNH_2BH_3

Inelastic neutron scattering (INS) spectrum was collected on the TOSCA beamline at the ISIS 2.3.4 at 20K (-253°C) for 8 hours. At room temperature KNH_2BH_3 crystallises in the orthorhombic space group *Pbca* with 16 molecules per unit cell each on a site of 8c symmetry as shown in Figure 6.2a. Each fundamental vibration of the isolated molecule gives rise to 128 factor group modes of the crystal.

To assign the spectra, density functional theory (DFT) calculations were performed on the complete unit cell using CASTEP [150, 151, 152]. Comparison of the observed and calculated bond distances for the complete unit cell with the experimental data shows good agreement: bond distances are generally within 0.02Å or 1.9%. The largest deviations are for the N-H bond lengths where the distances are 0.07Å longer than the observed experimental values. It was concluded that the *ab initio* calculations for the complete unit cell have accurately reproduced the experimental structure.

Figure 6.11 shows a comparison of the INS spectra calculated from the DFT results and the experimental spectrum. There is a reasonable agreement between the calculated and observed spectra and a complete list of all the observed bands and their assignments is provided in Appendix A, Table A.3. Nevertheless, there are two discrepancies which must be accounted for:

1. The DFT calculations overestimates most of the modes between 0-525cm^{-1}. The most pronounced irregularities are the lattice vibrations predicted at 231cm^{-1}, 288cm^{-1} and 318cm^{-1}(corresponding experimental modes at 177cm^{-1}, 235cm^{-1} and 251cm^{-1}) the BH_3 librational mode at 388cm^{-1} (experimental 354cm^{-1}). This is likely to have arisen from an overestimation of the electrostatic forces between the K^+ and the BH_3 units which are the stabilising factor of the extended structure. In the geometry optimised unit cell, the K atoms are shifted so the closest B-K distances decrease from 3.30Å to 3.07Å.

2. Two of the predicted modes at 636cm^{-1} and 697cm^{-1} are not present in the experimental data at all. Theoretically these modes correspond to NH_2 motion at the 2 and 1 sites respectively suggesting that presence of a second crystallographically distinct KNH_2BH_3 unit does not have a significant impact on the spectroscopic properties of the compound

Comparison of the KNH_2BH_3 and $LiNH_2BH_3$ INS spectra, Figure 6.12, provides further evidence that the vibrational modes of KNH_2BH_3 are dominated by its molecular motion. The peak positions are very similar with some splitting of the KNH_2BH_3 peaks showing slight shift conferred by the second site.

As with $LiNH_2BH_3$, the BH_3 librations of KNH_2BH_3 occur at lower energies (325cm^{-1}-405cm^{-1}) than the NH_2 librations (440cm^{-1}-504 cm^{-1}). This is the opposite of ammonia borane where the onset of NH_3 libration has been shown by NMR and quasielastic neutron scattering (QENS) [157] to have a lower activation energy than for BH_3. This change in behaviour is a consequence the close association of the K^+ and NH_2 in KNH_2BH_3. In this case, K^+ acts as an anchor for its end of the molecule because it takes more energy to overcome the electrostatic interactions and displace it.

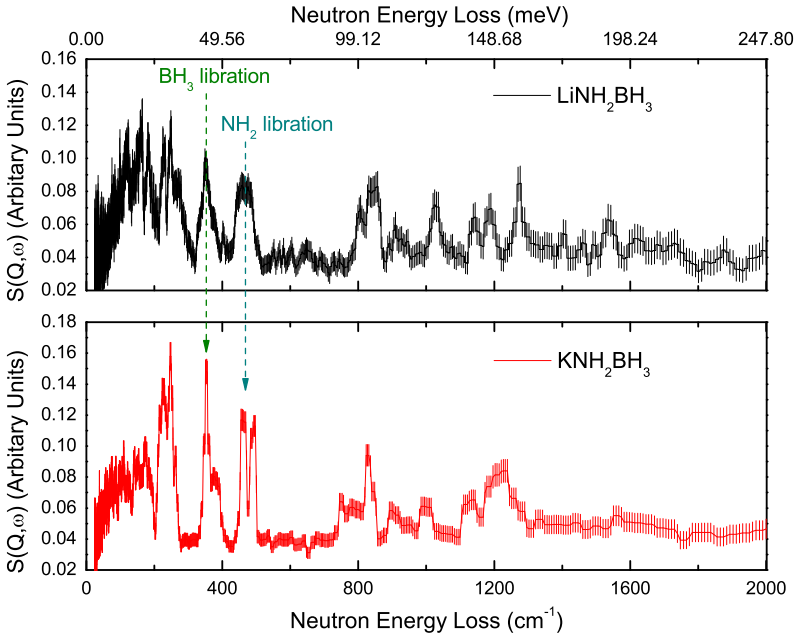

Figure 6.12: Comparison of experimental INS spectra: KNH_2BH_3 (red) and α-$LiNH_2BH_3$ (black) in the 0cm^{-1}-2000 cm^{-1} region.

The DFT calculations also revealed some surprising features. There are four imaginary modes at -255, -0.035, -0.034, -0.033cm^{-1} and additionally a low frequency real mode at 59 cm^{-1}. These correspond to shearing modes parallel the *a* axis along a central planar break with one half of the unit cell moving rigidly with respect to the other as shown in Figure 6.13. This is indicative of a very shallow double well potential for which the correct quantum nuclear solution in the an-harmonic potential still predicts zero displacement even at 0K. Negative phonon modes are often associated with a lowering of symmetry and their presence could indicate anomalous shearing behaviour if the cell is exposed to high pressure or very low temperature [194].

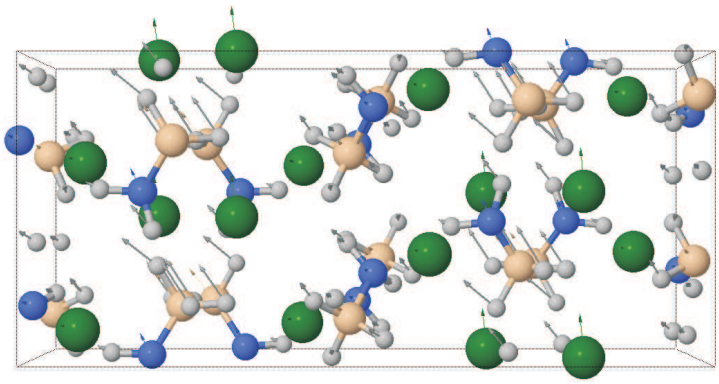

Figure 6.13: Structural diagram of KNH_2BH_3 viewing along the a axis showing the vector motion of the low energy mode at 59cm^{-1}. Potassium is green, nitrogen blue, and boron cream.

As described in Section 4.5 displacement tensors $^{\nu}B_l$ of an atom l vibrating in mode ν at temperature T in K can be calculated through Equation 6.1.

$$^{\nu}B_l =^{\nu} u_l^2 = \frac{16.9}{^{\nu}\mu_l\omega_\nu} coth\left(\frac{1.47\omega_\nu}{T}\right) \tag{6.1}$$

With the transition at ω in cm^{-1} and the reduced mass μ in atomic mass units, the atomic mean square is in Å^2. Hence the total mean square displacement of an atom at a given temperature can be calculated by summing the contributions of all the individual positive modes.

Figure 6.14 shows how the atomic motions of KNH_2BH_3 change with increasing temperature between 100K (-173°C) and its decomposition at 370K (97°C). Figure 6.15 gives a quantitative representation of these changes between 70K and 370K (-173°C and 97°C). As one would expect the amplitudes of the vibrations increase with temperature but perhaps surprisingly their directionality changes relatively little and the ellipsoids at 370K (97°C) are just expanded versions of those at 100K (-173°C). This lack of directionality is in contrast to findings for $LiNH_2BH_3$ (Section 4.5), were the Li motion becomes strongly orientated along the a axis, and is probably due to the difference in coordination geometry. As previously stated in Sections 2.2.2 and 4.2.1 the metal ions

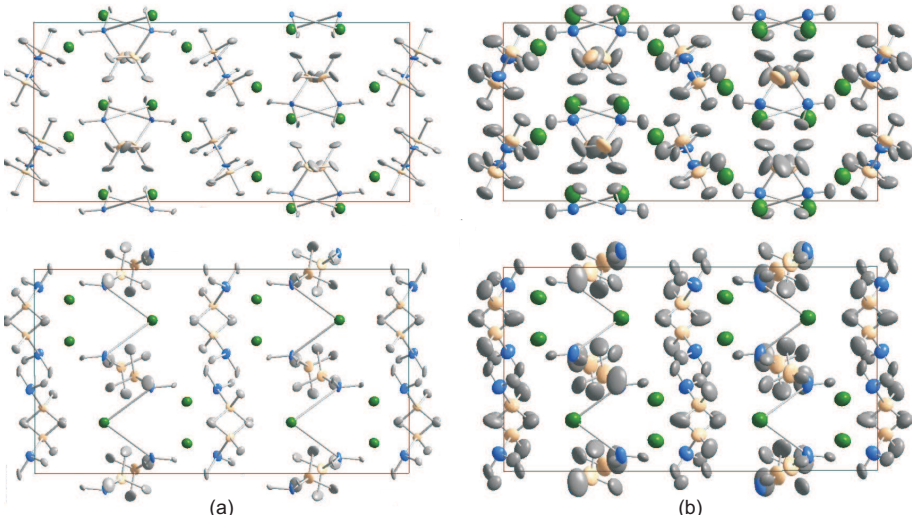

Figure 6.14: Structural diagrams of KNH_2BH_3 viewing along the *a* and *b* axis showing the total mean square displacement of the atoms at 100K (-173°C) (a)and 370K (97°C) (b)

are octahedrally coordinated in KNH_2BH_3 and tetrahedrally in $LiNH_2BH_3$. Octahedral coordination is more symmetric and as a result the intermolecular forces are more even and less polarisation occurs.

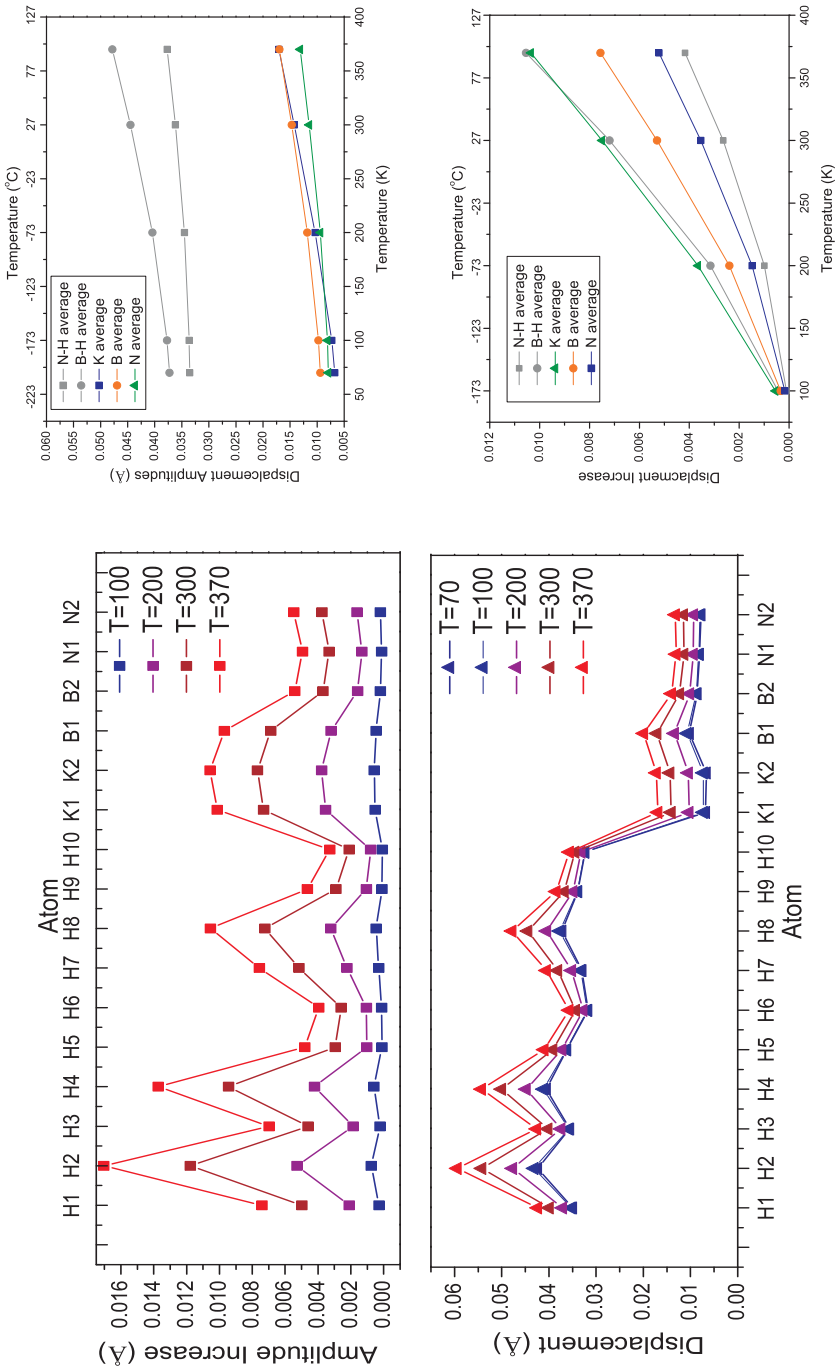

Figure 6.15: Graphs showing how the atomic displacements of KNH_2BH_3 change with temperature between 100K -370K (-173°C - 97°C).

6.5 Conclusions

KNH_2BH_3 was synthesised in a one pot room temperature reaction between KH and NH_3BH_3 in benzene. The structure of $KND_2{}^{11}BD_3$ was investigated by neutron powder diffraction and the structure of KNH_2BH_3 by synchrotron X-ray powder diffraction. The neutron and X-ray data were refined simultaneously and KNH_2BH_3 was identified to have the space group *Pbca* and room temperature lattice constants of a = 9.4304(1) Å, b = 8.2611(1) Å, and c = 17.3403(2)Å.

A variable temperature synchrotron X-ray diffraction study of KNH_2BH_3 was also completed. The lattice parameters of KNH_2BH_3 increased linearly with increasing temperature from 200K-335K (-73°C to 62°C) where upon the b axis began to deviate from the fit with a complete loss of crystallinity at 352K (79°C). It was postulated the reason for this was the orthogonal motion of the K1 and K2 sites along the a and c axes respectively.

A thermogravimetric analysis with mass spectrometry study of KNH_2BH_3 was performed. KNH_2BH_3 was heated to to 250 °C (673K) under 1 bar of flowing He (100ml min^{-1}). The sample lost 5.8% of its weight over two decomposition events. The events had maxima at 98°C (371K) and 180°C (453K) respectvly. The mass spectrometer detected hydrogen as the major decomosition product along with trace amounts of borazine, diborane and ammonia.

A DSC trace of KNH_2BH_3 was collected and showed a pre-decomposition endotherm at 67°C (340K) ΔH = +4.16 kJ mol^{-1}, a sharp decomposition exotherm at 71°C (340K), ΔH = -14.29 kJ mol^{-1} followed by a slow steady exotherm up to 175°C (448K).

A variable temperature neutron diffraction study of $KND_2{}^{11}BD_3$ with gravimetric analysis was performed. The lattice parameter of $KND_2{}^{11}BD_3$ increased linearly with increasing temperature from 303-350K (30-77°C)where upon they began to deviate from the fit with a complete loss of crystallinity at 358K (85°C). The sample of $KND_2{}^{11}BD_3$ lost 7.2% over the course of the experiment, of which, 0.3% was thought to be due to the desorption of physisorbed gas from powder grains and the remaining 6.9% was assigned to the $KND_2{}^{11}BD_3$ decomposition.

The peak mass loss occurred at 65°C, identified from the derivative of curve, and is significantly lower than the 98°C seen in the IGA-MS experiments (Section 6.3.1) *but* corroborates well with the loss of crystallinity observed in the variable temperature X-ray experiments (Section 6.3). These discrepancies are a prime example of how heating rate and sample volume have a significant impact on the apparent sample properties.

- The IGAn experiment was performed on a large sample (10ml volume) under vacuum, but had a very slow heating rate of 0.1 degree per hour. The very slow heating rate meant there was a long induction period and allowed the sample temperature to equilibrate thoroughly so decomposition could start at the lowest possible temperature.
- The IGA-MS experiment was performed on an medium sized sample 1ml volume under flowing gas. The sample was heated rapidly at 2°C min. A substantial sample and fast heating meant there was a significant time lag before the temperature equilibrated enough for the $KND_2{}^{11}BD_3$ to decompose.
- The X-ray diffraction experiment was performed on a very small sample volume (c.a. 500μl) within a sealed glass capillary. They were heated with an efficient cryostat at a fairly rapid heating rate of 1°C min. The small volume, sealed environment and efficient heating combined to ensure rapid temperature equilibration throughout the sample and no induction period was necessary before decomposition.
- The DSC experiment was again performed on a very small sample volume 250μl within an aluminium crucible. The nature of the experiment means efficient temperature equilibration is integral part despite the fairly rapid heating rate of 1°C min. Hence no induction period was observed.

The full phonon density of states was calculated by DFT which allowed comparison the INS spectrum collected. The calculations were also used to model the atomic motion up to the decomposition temperature of KNH_2BH_3.

Chapter 7

Conclusions and Further Work

7.1 Thesis Summary

To summarise, this thesis principally involved the investigation of B-N-H containing materials for hydrogen storage applications with a particular emphasis on alkali-metal amidoboranes. Their hydrogen storage properties were assessed by thermogravimetric analysis, variable temperature X-ray and neutron diffraction and inelastic neutron scattering. Particular highlights include

- The variable temperature INS spectra of $NH_3{}^{11}BH_3$ and α-$LiNH_2BH_3$,
- Low temperature INS spectra of aged-$NaNH_2BH_3$ and KNH_2BH_3.
- Identification of the structural phase transitions of ND_4BD_4.
- The 'one pot' synthesis of α-$LiNH_2BH_3$, $NaNH_2BH_3$ and KNH_2BH_3 from the reaction of NH_3BH_3 and the appropriate metal hydride in diethyl ether or benzene.
- The detailed characterisation of structures and thermal behaviour of the alkali metal amidoboranes α-$LiNH_2BH_3$, a lithiated tetragonal phase, β-$LiNH_2BH_3$, $NaNH_2BH_3$ and KNH_2BH_3.

Inelastic neutron scattering (INS) spectra were collected on $NH_3{}^{11}BH_3$ at eight temperatures between 25-280K (-248°C to 7°C). The full phonon density of states was calculated by DFT and used to assign the spectra and the relative onset of the NH_3 and BH_3 librations were correlated to their moments of inertia. Analysis of the changes in

peak intensity associated with NH_3 and BH_3 libration supported the findings of Cho *et al.* [156] that NH_3 libration has an earlier onset than the BH_3. Exponential regions of the 240K and 280K (-33°C and 7°C) spectra were assigned as boson peaks, attributed to almost free rotation of the NH_3 end of the molecule.

The structure of $ND_4{}^{11}BD_4$ was investigated by variable temperature neutron powder diffraction between 2K and 200K (-271°C and -73°C). Three progressively more ordered phases where identified, whose formation depended strongly on the 'thermal history' of the sample. Above 60K (-213°C), $ND_4{}^{11}BD_4$ has a rock-salt structure with the BD_4 and ND_4 units 2 and 48 fold disordered respectively. The cubic lattice parameters were fitted with a polynomial function with terms involving Debye [136] and Einstein [170] models of thermal expansion. Slow cooling below 60K allowed a cubic - rhombohedral phase change across two body diagonals of the cubic cell, the BD_4 and ND_4 units were 0 and 12 fold disordered respectively. Slow cooling below 40K was accompanied by a rhombohedral - trigonal phase change which doubled the *a* and *b* axes of the rhombohedral cell, the BD_4 and ND_4 units were ordered and 3-fold disordered respectively. Heat capacity measurements confirmed the phase change behaviour.

Two phases of $LiNH_2BH_3$ (α and β) have been identified and their structures solved. Both structures were found to be orthorhombic *Pbca* with tetrahedrally coordinated Li^+. However the β phase has two different lattice sites and a larger unit cell. During variable temperature X-ray diffraction experiments, α-$LiNH_2BH_3$ exhibited anisotropic thermal expansion with a complete loss of crystallinity at 94°C/367K. Thermogravimetric and DSC analysis showed α-$LiNH_2BH_3$ to decompose in two exothermic stages (92°C/365K and 110°C/383K under 1 bar flowing helium). The majority of the gas released was hydrogen with only trace amounts of NH_3 were observed during the first stage of decomposition. The full phonon density of states was calculated by DFT which allowed comparison with the INS spectra (collected on TOSCA and MAPS) and the Raman spectrum. The calculations were also used to model the atomic motion up to the decomposition temperature of α-$LiNH_2BH_3$. Combination of the crystallographic, thermogravimetric and vibrational information allowed a mechanism to be proposed for the decomposition of α-$LiNH_2BH_3$.

A lithiated tetragonal phase was made from the solid state reaction of LiH and NH_3BH_3 in a 1:2 ratio. The crystal structure was partially solved from X-ray and neutron data with the aid of solid sate 11B NMR and an *in situ* synthesis in the IGA. The decomposition of the lithiated tetragonal phase was also studied by thermogravimetric analysis with mass spectrometry and occurred over two decomposition events. The events had maxima at 144°C (417K)and 239°C (512K). INS and Raman spectra were collected and general regions of the spectra were identified.

The structure of $NaNH_2BH_3$ was found to be isostructural with α-$LiNH_2BH_3$ but with expanded lattice constants. During variable temperature X-ray diffraction experiments, $NaNH_2BH_3$ exhibited anisotropic thermal expansion with a complete loss of crystallinity at 78°C/351K. Thermogravimetric analysis showed $NaNH_2BH_3$ to decompose in two exothermic stages (78°C/351K and 167°C/440K under 1 bar flowing helium). The majority of the gas released was hydrogen with only trace amounts of NH_3 and B_2H_6 during the first stage of decomposition. $NaNH_2BH_3$ was found to be highly susceptible to degradation by radiation which decomposes it to NaH and an amorphous compound and also ages, transforming to an amorphous compound over a period of weeks.

The structure of KNH_2BH_3 was also found to be orthorhombic *Pbca* but the K is octahedrally coordinated and there are two distinct KNH_2BH_3 units. During variable temperature X-ray diffraction experiments KNH_2BH_3 exhibited anisotropic thermal expansion with a complete loss of crystallinity at 79°C/352K. Thermogravimetric and DSC analysis showed KNH_2BH_3 to decompose in two exothermic stages (98°C/371K and 180°C/458K under 1 bar flowing helium) with a pre-decomposition endotherm at 67°C (340K). The majority of the gas released was hydrogen with only trace amounts of NH_3, B_2H_6 and $N_3B_3H_6$ released. Heating rate and sample volume were found to have a large effect on the decomposition properties observed indicating poor thermal conductivity for this phase. The full phonon density of states was calculated by DFT which allowed comparison the INS spectrum collected. The calculations were also used to model the atomic motion up to the decomposition temperature of KNH_2BH_3.

Table 7.1: Key bond lengths for the metal amidoboranes in this thesis.

	NH_3BH_3	α-$LiNH_2BH_3$	$NaNH_2BH_3$	KNH_2BH_3
Unit cell	orthorhombic	orthorhombic	orthorhombic	orthorhombic
Space Group	*Pmn21*	*Pbca*	*Pbca*	Pbca
M^+ coordination	-	Tetrahedral	Tetrahedral	Octahedral
B-N	1.582(5)	1.542(4)	1.543(6)	1.540(6)
N-M	1.07(4)	1.99(4)	2.32(3)	3.02(3)
N-H	0.96(3)	0.99(2)	1.03(1)	1.04(2)
B-H	1.18, 1.15(4)	1.22(2)	1.22(1)	1.24(2)
B-M	-	2.62	2.87	3.32

7.2 Structure

Sensitivity is a key word when discussing the structural chemistry of the ammonia borane derivatives described in this thesis. Their sensitivity is manifested in their:

- polymorphism - α-$LiNH_2BH_3$, β-$LiNH_2BH_3$, the lithiated tetragonal phase and the three phases of $ND_4{}^{11}BD_4$
- aging - degradation over time of $NaNH_2BH_3$ to an amorphous compound and NaH
- susceptibility to radiation damage - α-$LiNH_2BH_3$ and $NaNH_2BH_3$ at the ESRF
- highly measurement dependent properties - KNH_2BH_3

This structural 'softness' must be due to their dependence (with the exception of $ND_4{}^{11}BD_4$) on the relatively weak $M^+ \cdots H^{\delta-}$ interactions. The closest intermolecular $H^{\delta+} \cdots H^{\delta-}$ distances to increase from 1.96Å(NH_3BH_3) to 2.37Å α-$LiNH_2BH_3$, close to the expected van-der-Waals distance and too far for the significant $H^{\delta+} \cdots H^{\delta-}$ interactions to occur.

Table 7.1 summaries the key structural features for NH_3BH_3, α-$LiNH_2BH_3$ $NaNH_2BH_3$ and KNH_2BH_3. As would be expected the M-N bonds lengthen down the group in accordance with the increasing M^+ radius. But once the N-H has been replaced by the N-M, the $[NH_2BH_3]^-$ changes relatively little down the group.

Initial changes between NH_3BH_3 and M-NH_2BH_3 to the $[NH_2BH_3]^-$ are however significant. The B-N bond decreases because the ionic nature of M-NH_2BH_3 increases the electron density on the nitrogen. This increases the availability of the lone pair and the Lewis basicity of the nitrogen, allowing greater electron donation to the Lewis acid BH_3 unit, resulting in a stronger, shorter bond. There is no change between the Li and Na B-N bonds but the K B-N is slightly shorter still, potentially due to the octahedral coordination and weaker N-M interactions.

The shorter B-N bonds are mainly at the expense of the B-H bonds due to the increased electron density on the boron from the more available nitrogen lone pair. Consequently, there is a decrease its affinity for the electrons centred on the $H^{\delta-}$, resulting in a weaker, longer bond. The N-H bond lengthens slightly probably due to increased steric repulsion from the $[M]^+$ and also gets longer down the group.

For $ND_4{}^{11}BD_4$ the situation is different again. There is no B-N bond, the closest distance is 3.435Å and the intermolecular interactions are electrostatic between the $[ND_4]^+$ and the $[BD_4]^-$ unit. The dihydrogen interactions once again reign supreme with the closest intermolecular $H^{\delta+} \cdots H^{\delta-}$ of 1.953Å even shorter than that of NH_3BH_3 (1.96Å). At 1.05Å and 1.23Å respectively the N-D bonds and B-D are longer than those of NH_3BH_3 (0.96 and 1.18Å respectively) due to the charge being shared out over 4 not 3 bonds.

7.3 Decomposition

Determining the absolute decomposition temperatures for the alkali metal amidoboranes is a complex process. The findings are highly dependent on the synthesis method used, the heating rate and the sample volume. As previously discussed in Section 6.5, KNH_2BH_3 was particularly challenging in this respect and it is thought that the sample may have considerably lower thermal conductivity than the other metal amidoboranes.

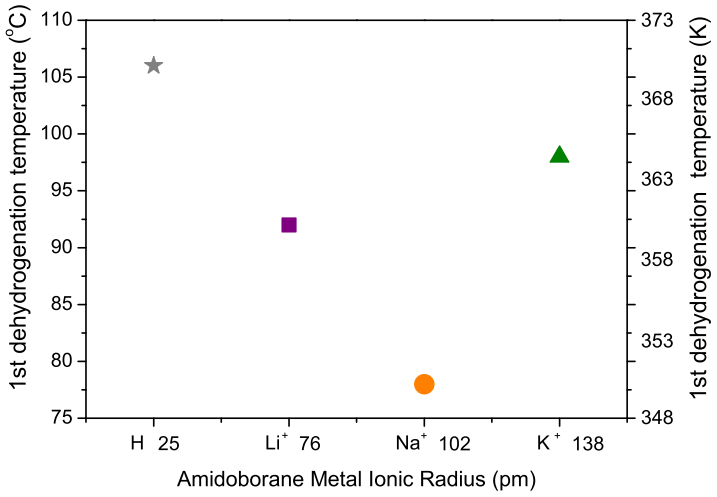

Figure 7.1: A plot of the 1st dehydrogenation temperature vs. the amidoborane metal ionic radius

Nevertheless, it has been possible to compare different samples within the same measurement technique. Figure 7.1 shows the peak hydrogen desorption temperature for NH_3BH_3, α-$LiNH_2BH_3$, $NaNH_2BH_3$ and KNH_2BH_3 as determined by the thermogravimetric analysis with mass spectrometry. All samples were heated at 2°C minute under 1 bar of flowing He.

Replacement of a single H in NH_3BH_3 with a Li reduces the the peak H_2 evolution from 106°C/379K to 92°C/365K due to the interruption of the dihydrogen bonding and the lengthening/weakening of the B-H and N-H bonds, see Section 7.2. Replacement of Li by Na lowers the decomposition temperature still further to 78°C/351K. This is because the increased Na radius forces the amidoborane units further apart so the weakening the van der Waals forces that hold the structure together.

Following the same trend substitution, KNH_2BH_3 might be predicted to have a lower decomposition temperature than $NaNH_2BH_3$ as with the analogous alkali metal borohydrides [210]. However at 98°C/371K it has the highest decomposition temperature of all the alkali metal amidoboranes. This increase is a consequence of the change on coordination geometry from tetrahedral to octahedral. At 138pm the K^+ ion is too

large to be fully stabilised by a tetrahedral coordination and requires the extra stability conferred by octahedral coordination. As the coordination number has changed from 4 to 6 then the number of intermolecular forces which must be overcome before the sample can decompose has gone up by a third.

7.4 Further Work

7.4.1 Continuation of Thesis Research

Future work on the alkali metal amidoboranes and ammonium borohydride should focus on learning more about the behaviour of the new structures discussed in this thesis and gaining an even greater understanding of the decomposition pathways of all of these compounds.

A more detailed variable temperature neutron diffraction study should be undertaken on $ND_4{}^{11}BD_4$ using the WISH beamline at ISIS. Data should be collected for longer over a wider temperature range (2-200K) to allow more accurate modeling of the progressive ordering. To gain a more complete understanding of the dynamics involved in the phase transitions variable temperature INS should be performed and the full phonon density of states calculated for all three phases so as to fully assign the phonon modes. Molecular dynamics calculations should also be performed to allow the most energetically favourable ground state structure to be found.

The low energy shearing modes in the DFT calculations on α-$LiNH_2BH_3$ and KNH_2BH_3 indicate that a monoclinic phase transitions could be induced at very low temperatures or high pressures. It would be of fundamental interest to conduct synchrotron diffraction experiments under these conditions to see if such changes occur.

The crystal structure of the lithiated tetragonal phase needs to be fully optimised. The optimized structure should then be used to calculate the full phonon density of states for the lithiated tetragonal phase to allow complete assignment of the experimental INS spectrum. It would also be of interest to heat the sample up in an open system to see if the $LiBH_4$ would form during heating and hopefully confirm the presence of the LiH-BH_3 adduct. Variable temperature solid state ^{11}B NMR of both the formation

and decomposition would also be beneficial to identify some of the reaction intermediates.

The structures of α-$LiNH_2BH_3$, $NaNH_2BH_3$ and KNH_2BH_3 are all well characterised but, as with the lithiated tetragonal phase, NMR is important for further research. Firstly, time resolved studies of the reactions in solution would be an effective way to confirm the proposed reaction routes. Secondly, variable temperature decomposition studies should be made to determine the various potential intermediates and allow more definite decomposition mechanisms to be elucidated. PDF analysis of the decomposed products would also be helpful to obtain more information about the amorphous polymeric products formed.

The synthesis of β-$LiNH_2BH_3$ should be optimised so that it can be made reliably phase pure. This would allow its decomposition properties to be characterised more accurately and more comparisons could be made with α-$LiNH_2BH_3$.

7.4.2 General Ammonia Borane Derivatives for Hydrogen Storage

Of all the compounds studied in this thesis α-$LiNH_2BH_3$ is the one with the most potential as a hydrogen storage material. Presently, none of the ammonia borane derivatives discussed in this thesis cannot be used in reversible hydrogen storage systems due to their poor reversibility of the dehydrogenation reaction. Apart from the issue of reversibility, α-$LiNH_2BH_3$ has the highest weight percent hydrogen, ambient temperature, long term stability, non toxic emissions and high purity bulk synthesis. The other ammonia borane derivatives all suffer from additional drawbacks e.g.

- lower weight percent hydrogen ($NaNH_2BH_3$, KNH_2BH_3),
- thermal instability ($ND_4{}^{11}BD_4$),
- aging ($NaNH_2BH_3$),
- paralax (KNH_2BH_3),
- higher proportions of unwanted gas emission ($NaNH_2BH_3$, the lithiated tetragonal phase)
- difficult synthesis ($ND_4{}^{11}BD_4$, β-$LiNH_2BH_3$)

However, work by Burrell *et al.* [50] on the regeneration of spent NH_3BH_3 offers hope that a regeneration pathway for α-$LiNH_2BH_3$ may be found. Their 'one pot' method, described in more detail in Section 1.3.2, should be tried with spent α-$LiNH_2BH_3$, and if preliminary tests show promise attempts should be made to optimise the reaction.

Other methods used to aid the decomposition and regeneration of NH_3BH_3 should also be investigated for α-$LiNH_2BH_3$. In particular doping with nano-particles and nano-confinement which proved to be successful for NH_3BH_3 (Section 1.4). The most efficient way to investigate the large number of possibilities these modifications present would be to use a combinatorial approach and it is here that a collaboration between the University of Oxford, the Rutherford Appleton Laboratory (RAL), Johnson Matthey and Ilika Technologies could be extremely powerful. A high throughput solid state testing robot has been developed that is capable of following the decomposition (with gas analysis) of 50 separate reactions simultaneously. This would allow many different types, and loadings, of catalytic materials to be tested very rapidly and permit swift identification of the most promising combinations.

Some research into NH_3BH_3 for use in a direct fuel cell has also been performed [211] and it would be very interesting to investigate the electrochemical properties of α-$LiNH_2BH_3$. The added conductivity of the Li^+ ion may also provide an alternative route for regeneration.

Ammonia borane and its derivatives are part of a diverse, dynamic research area and they are still considered highly promising candidates as hydrogen storage materials. However, there are some aspects which must be solved if they are to complete the transition from 'promising' to 'commercially viable'. Chiefly regeneration of the spent fuel. In recognition of this, research into this area is gathering momentum. Once the regeneration is solved, I believe there is very little to stand in the way of ammonia borane becoming a key part of the hydrogen economy.

Bibliography

[1] K. R. Ryan, A. J. Ramirez-Cuesta, K. Refson, M. O. Jones, P. P. Edwards, W. I. David, *Physical Chemistry Chemical Physics*, 2011, **Accepted**.

[2] L. Carnot, Sadi. Nicolas, R. H. Thurston, H. Carnot, W. T. Kelvin, *Reflections on the Motive Power of Heat and on Machines Fitted to Develop that Power: From the Original French of N.L.S. Carnot*, J. Wiley Sons, 1890.

[3] U. D. O. Energy, *DOE Targets for Onboard Hydrogen Storage Systems for Light-Duty Vehicles*, 2009.

[4] L. Schlapbach, A. Zuttel, *Nature*, 2001, **414**, 353–358.

[5] J. L. C. Rowsell, O. M. Yaghi, *Angewandte Chemie-International Edition*, 2005, **44**, 4670–4679.

[6] W. Grochala, P. P. Edwards, *Chemical Reviews*, 2004, **104**, 1283–1315.

[7] G. Sandrock, *Journal of Alloys and Compounds*, 1999, **295**, 877–888.

[8] E. A. Nickels, M. O. Jones, W. I. F. David, S. R. Johnson, R. L. Lowton, M. Sommariva, P. P. Edwards, *Angewandte Chemie-International Edition*, 2008, **47**, 2817–2819.

[9] B. Bogdanovic, M. Schwickardi, *Journal of Alloys and Compounds*, 1997, **253**, 1–9.

[10] P. Chen, Z. T. Xiong, J. Z. Luo, J. Y. Lin, K. L. Tan, *Nature*, 2002, **420**, 302–304.

[11] R. L. Lowton, M. O. Jones, W. I. F. David, S. R. Johnson, M. Sommariva, P. P. Edwards, *Journal of Materials Chemistry*, 2008, **18**, 2355–2360.

[12] X. P. Zheng, X. H. Qu, I. S. Humail, P. Li, G. Q. Wang, *International Journal of Hydrogen Energy*, 2007, **32**, 1141–1144.

[13] F. H. Stephens, V. Pons, R. T. Baker, *Dalton Transactions*, 2007, 2613–2626.

[14] C. F. Lane, *Ammonia-Borane and Related N-B-H Compounds and Materials: Safety Aspects, Properties and Applications*, Tech. Rep., Northern Arizona University, 2006.

[15] K. D. M. Harris, P. P. E. Edwards, *Turning Points in Solids State, Materials and Surface Science*, 2008, **Royal Society of Chemistry,**, Chapter 4, pp.51–75,.

[16] P. W. Atkins, J. De Silva, *Physical Chemistry 7th Edition*, Oxford University Press, 2002.

[17] J. Emsley, *Chemial Society Reviews*, 1980, **9**, 91–124.

[18] I. Alkorta, I. Rozas, J. Elguero, *Chemical Society Reviews*, 1998, **27**, 163.

[19] J. Wessel, J. C. Lee, E. Peris, G. P. A. Yap, J. B. Fortin, J. S. Ricci, G. Sini, A. Albinati, T. F. Koetzle, O. Eisenstein, A. L. Rheingold, R. H. Crabtree, *Angewandte Chemie International Edition in English*, 1995, **34**, 2507.

[20] D. Hugas, S. Simon, M. Duran, *The Journal of Physical Chemistry A*, 2007, **111**, 4506–4512.

[21] S. Trudel, D. F. R. Gilson, *Inorganic Chemistry*, 2003, **42**, 2814–2816.

[22] J. S. Li, F. Zhao, F. Q. Jing, *Journal of Chemical Physics*, 2002, **116**, 25–32.

[23] I. Rozas, I. Alkorta, E. J., *Chemical Physics Letters*, 1997, **275**, 423–428.

[24] S. G. Shore, R. W. Parry, *Journal of the American Chemical Society*, 1955, **77**, 6084–6085, 4.

[25] E. L. Lippert, W. N. Lipscomb, *Journal of the American Chemical Society*, 1956, **78**, 503–504.

[26] E. W. Hughes, *Journal of the American Chemical Society*, 1956, **78**, 502–503.

[27] D. J. Heldebrant, A. Karkamkar, J. C. Linehan, T. Autrey, *Energy Environmental Science*, 2008, **1**, 156–160.

[28] A. Staubitz, A. Robertson, I. Manners, *Chemistry Review*, 2010, **110**, 4079–4124.

[29] V. P. Sorokin, B. I. Vesnina, N. S. Klimova, *Zhurnal Neorganicheskoi Khimii*, 1963, **8**, 66–68.

[30] C. F. Hoon, E. C. Reynhardt, *Journal of Physics C-Solid State Physics*, 1983, **16**, 6129–6136.

[31] M. E. Bowden, G. J. Gainsford, W. T. Robinson, *Australian Journal of Chemistry*, 2007, **60**, 149–153.

[32] W. T. Klooster, T. F. Koetzle, P. E. M. Siegbahn, T. B. Richardson, R. H. Crabtree, *Journal of the American Chemical Society*, 1999, **121**, 6337–6343.

[33] J. B. Yang, J. Lamsal, Q. Cai, W. J. James, W. B. Yelon, *Applied Physics Letters*, 2008, **92**.

[34] N. J. Hess, M. E. Bowden, V. M. Parvanov, C. Mundy, S. M. Kathmann, G. K. Schenter, T. Autrey, *Journal of Chemical Physics*, 2008, **128**.

[35] Y. Filinchuk, A. Nevidomskyy, D. Chernyshov, V. Dmitriev1, *Physical Review B*, 2009, **79**, 214111.

[36] R. Custelcean, Z. A. Dreger, *Journal of Physical Chemistry B*, 2003, **107**, 9231–9235.

[37] Y. Lin, W. L. Mao, V. Drozd, J. Chen, L. L. Daemen, *Journal of Chemical Physics*, 2008, **129**.

[38] T. B. Richardson, S. deGala, R. H. Crabtree, P. E. M. Siegbahn, *Journal of the American Chemical Society*, 1995, **117**, 12875–12876.

[39] P. M. Kuznesof, D. F. Shriver, F. E. Stafford, *Journal of the American Chemical Society*, 1968, **90**, 2557.

[40] C. R. Miranda, G. Ceder, *Journal of Chemical Physics*, 2007, **126**, 11.

[41] A. C. Stowe, W. J. Shaw, J. C. Linehan, B. Schmid, T. Autrey, *Physical Chemistry Chemical Physics*, 2007, **9**, 1831–1836.

[42] D. J. Heldebrant, A. Karkamkar, N. J. Hess, M. Bowden, S. Rassat, F. Zheng, K. Rappe, T. Autrey, *Chemistry of Materials*, 2008, **20**, 5332–5336.

[43] O. Palumbo, A. Paolone, P. Rispoli, R. Cantelli, T. Autrey, *Journal of Power Sources*, 2010, **195**, 1615.

[44] J. Nyln, T. Sato, E. Soignard, J. L. Yarger, E. Stoyanov, *The Journal of Chemical Physics*, 2009, **131**, 104506.

[45] P. V. Ramachandran, P. D. Gagare, *Inorganic Chemistry*, 2007, **46**, 7810–7817.

[46] L. G. Sneddon, *DoE Hydrogen Annual Progress Report*, 2007, Amineborane Hydrogen Storage – New Methods for Promoting Amineborane Dehydrogenation/Regeneration Reactions.

[47] S. Hausdorf, F. Baitalow, G. Wolf, F. O. R. L. Mertens, *Int. J. Hydrogen Energy*, 2008, **33**, 608.

[48] B. Davis, D. Dixon, E. Garner, J. Gordon, M. Matus, B. Scott, F. Stephens, *Angewandte Chemie International Edition*, 2009, **48**, 6812.

[49] A. D. Sutton, B. L. Davis, K. X. Bhattacharyya, B. D. Ellis, J. C. Gordon, P. P. Power, *Chem. Commun*, 2010, **46**, 148.

[50] A. K. Burrell, J. C. Gordon, K. Sutton, A. Ott, *US Patent*, 2010, **20100272622**.

[51] T. Autrey, A. Gutowska, L. Y. Li, J. C. Linehan, M. Gutowski, *Abstracts of Papers of the American Chemical Society*, 2004, **227**, 062–FUEL.

[52] A. Gutowska, L. Y. Li, Y. S. Shin, C. M. M. Wang, X. H. S. Li, J. C. Linehan, R. S. Smith, B. D. Kay, B. Schmid, W. Shaw, M. Gutowski, T. Autrey, *Angewandte Chemie-International Edition*, 2005, **44**, 3578–3582.

[53] A. Paolone, O. Palumbo, P. Rispoli, R. Cantelli, T. Autrey, A. Karkamkar, *Journal of Physical Chemistry C*, 2009, **113**, 10319–10321.

[54] A. Feaver, S. Sepehri, P. Shamberger, A. Stowe, T. Autrey, G. Z. Cao, *Journal of Physical Chemistry B*, 2007, **111**, 7469–7472.

[55] Z. Kurban, A. Lovell, S. M. Bennington, D. W. K. Jenkins, K. R. Ryan, M. O. Jones, N. T. Skipper, W. I. F. David, *Journal of Physical Chemistry C*, **114**.

[56] C. A. Jaska, K. Temple, A. J. Lough, I. Manners, *Chemical Communications*, 2001, **11**, 962.

[57] M. C. Denney, V. Pons, T. J. Hebden, D. M. Heinekey, K. I. Goldberg, *Journal of the American Chemical Society*, 2006, **128**, 12048–12049.

[58] T. M. Douglas, A. B. Chaplin, A. S. Weller, X. Z. Yang, M. B. Hall, *Journal of the American Chemical Society*, 2009, **131**, 15440–15456.

[59] T. Umegaki, J. M. Yan, X. B. Zhang, H. Shioyama, N. Kuriyama, Q. Xu, *International Journal of Hydrogen Energy*, 2009, **34**, 3816–3822.

[60] C. Y. Tang, A. L. Thompson, S. Aldridge, *Journal of the American Chemical Society*, 2010, **132**, 10578–10591.

[61] S. C. Li, M. S. Zhao, Y. Z. Wang, J. Zhai, *Materials Chemistry and Physics*, 2009, **118**, 51–56.

[62] J. M. Yan, X. B. Zhang, H. Shioyama, Q. Xu, *Journal of Power Sources*, 2009, **195**, 1091–1094.

[63] T. He, Z. Xiong, G. Wu, H. Chu, C. Wu, T. Zhang, P. Chen, *Chemistry of Materials*, 2009, **21**, 2315–2318.

[64] S. B. Kalidindi, J. Joseph, B. R. Jagirdar, *Energy and Environmental Science*, 2009, **2**, 1274–1276.

[65] U. B. Demirci, P. Miele, *Journal of Power Sources*, 2010, **195**, 4030 – 4035.

[66] A. Paul, C. Musgrave, *Angewandte Chemie International Edition*, 2007, **46**, 8153.

[67] R. J. Keaton, J. M. Blacquiere, R. T. Baker, *Journal of the American Chemical Society*, 2007, **129**, 1844.

[68] X. Yang, M. B. Hall, *Journal of the American Chemical Society*, 2008, **130**, 1798–1799.

[69] P. M. Zimmerman, A. Paul, Z. Zhang, C. B. Musgrave, *Angewandte Chemie International Edition*, 2009, **48**, 2201.

[70] V. Pons, R. T. Baker, N. K. Szymczak, D. J. Heldebrant, J. C. Linehan, M. H. Matus, D. J. Grant, D. A. Dixon, *Chemical Communications*, 2008, **48**, 6597.

[71] F. H. Stephens, R. T. Baker, M. H. Matus, D. J. Grant, D. A. Dixon, *Angewandte Chemie International Edition*, 2007, **46**, 746.

[72] A. J. M. Miller, J. E. Bercaw, *Chemical Communications*, 2010, **46**, 1709–1711.

[73] Y. Guo, X. He, Z. Li, Z. Zou, *Inorganic Chemistry*, 2010, **49**, 3419–3423.

[74] M. E. Bluhm, M. G. Bradley, R. Butterick, U. Kusari, L. G. Sneddon, *Journal of the American Chemical Society*, 2006, **128**, 7748–7749.

[75] Q. Xu, M. Chandra, *Journal of Power Sources*, 2006, **163**, 364–370.

[76] M. Chandra, Q. Xu, *Journal of Power Sources*, 2007, **168**, 135–142.

[77] R. P. Shrestha, H. V. K. Diyabalanage, T. A. Semelsberger, K. C. Ott, A. K. Burrell, *International Journal of Hydrogen Energy*, 2009, **34**, 2616–2621.

[78] X. Zhang, J. Yan, S. Han, H. Shioyama, Q. Xu, *Journal of the American Chemical Society*, 2009, **131**, 2778–2779.

[79] M. Zahmakiran, S. Özkar, *Applied Catalysis B: Environmental*, 2009, **89**, 104 – 110.

[80] M. Zahmakiran, F. Durap, S. Özkar, *International Journal of Hydrogen Energy*, 2010, **35**, 187 – 197.

[81] M. Rakap, S. Özkar, *International Journal of Hydrogen Energy*, 2010, **35**, 1305 – 1312.

[82] H. B. Dai, D. Z. Kang, P. Wang, *International Journal of Hydrogen Energy*, 2010, **35**, 10317 – 10323.

[83] Y. Q. Li, L. Xie, Y. Li, J. Zheng, X. G. Li, *Chemistry-a European Journal*, 2009, **15**, 8951–8954.

[84] D. Neiner, A. Karkamkar, J. C. Linehan, B. Arey, T. Autrey, S. M. Kauzlarich, *The Journal of Physical Chemistry C*, 2009, **113**, 1098–1103.

[85] Z. Li, G. Zhu, G. Lu, S. Qiu, X. Yao, *Journal of the American Chemical Society*, 2010, **132**, 1490–1491.

[86] Z. T. Xiong, C. K. Yong, G. T. Wu, P. Chen, W. Shaw, A. Karkamkar, T. Autrey, M. O. Jones, S. R. Johnson, P. P. Edwards, W. I. F. David, *Nature Materials*, 2008, **7**, 138–141.

[87] C. Wu, G. Wu, Z. Xiong, W. I. F. David, K. R. Ryan, M. O. Jones, P. P. Edwards, H. Chu, P. Chen, *Inorg. Chem.*, 2010, **49**, 4319–4323.

[88] W. I. F. David, K. R. Ryan, M. O. Jones, C. Wu, G. Wu, Z. T. Xiong, P. Chen, *Acta Crystallographica E*, 2011, **Submitted**.

[89] H. V. K. Diyabalanage, T. Nakagawa, R. P. Shrestha, T. A. Semelsberger, B. L. Scott, A. K. Burrell, W. I. F. David, K. R. Ryan, M. O. Jones, P. P. Edwards, *Journal of the American Chemical Society*, 2010, **132**, 11836–11837.

[90] H. V. K. Diyabalange, R. P. Shrestha, T. A. Semelsberger, B. L. Scott, M. E. Bowden, A. K. Burrell, *Angewandte Chemie, International Edition*, 2007, **46**, 8995–8997.

[91] H. Wu, W. Zhou, T. Yildirim, *Journal of the American Chemical Society*, 2008, **130**, 14834–14839.

[92] R. V. Genova, K. J. Fijalkowski, A. Budzianowski, W. Grochala, *Journal of Alloys and Compounds*, 2010, **499**, 144 – 148.

[93] Y. S. Chen, J. L. Fulton, J. C. Linehan, T. Autrey, *Journal of the American Chemical Society*, 2005, **127**, 3254–3255.

[94] D. J. Grant, M. H. Matus, K. D. Anderson, D. M. Camaioni, S. R. Neufeldt, C. F. Lane, D. A. Dixon, *Journal of Physical Chemistry A*, 2009, **113**, 6121–6132.

[95] C. H. Sun, X. D. Yao, A. J. Du, L. Li, S. Smith, G. Q. Lu, *Physical Chemistry Chemical Physics*, 2008, **10**, 6104–6106.

[96] K. J. Fijakowski, W. Grochala, *Journal of Materials Chemistry*, 2009, **19**, 2043–2050.

[97] Z. T. Xiong, G. T. Wu, Y. S. Chua, J. J. Hu, T. He, W. L. Xu, P. Chen, *Energy Environmental Science*, 2008, **1**, 360–363.

[98] J. Spielmann, M. Bolte, S. Harder, *Chem. Commun.*, 2009, 6934–6936.

[99] Y. S. Chua, G. Wu, Z. Xiong, A. Karkamkar, J. Guo, M. Jian, M. W. Wong, T. Autrey, P. Chen, *Chemical Communications*, 2010, **46**, 5752–5754.

[100] Q. Zhang, C. Tang, C. Fang, F. Fang, D. Sun, L. Ouyang, M. Zhu, *The Journal of Physical Chemistry C*, 2010, **114**, 1709–1714.

[101] M. S. Hill, G. Kociok-Kohn, T. P. Robinson, *Chemical Communications*, 2010, **46**, 7587.

[102] R. W. Parry, G. Kodama, D. R. Schultz, *Journal of the American Chemical Society*, 1958, **80**, 24–27.

[103] M. Krumpolc, *AIP Conference Proceedings*, 1983, 502–504.

[104] D. A. Dixon, M. Gutowski, *Journal of Physical Chemistry A*, 2005, **109**, 5129–5135.

[105] A. Karkamkar, S. M. Kathmann, G. K. Schenter, D. J. Heldebrant, N. Hess, M. Gutowski, T. Autrey, *Chem. Mater.*, 2009, **21**, 4356–4358.

[106] R. Jenkins, R. L. Snyder, *Introduction to X-ray Powder Diffractometry*, Wiley Interscience„ 1996.

[107] W. L. Bragg, *Proceedings of the Cambridge Philosophical Society*, 1913, **17**, 43–57.

[108] C. Kittel, *Introduction to Solid State Physics*, John Wiley Sons New York„ 1976.

[109] P. Ewald, *Annalen der Physik*, 1917, **54**, 519.

[110] A. K. Cheetham, P. Day, *Solid State Chemistry Techniques*, Clarendon Press Oxford„ 1978.

[111] M. M. Woolfson, *Reports on Progress in Physics*, 1971, **34**, 369.

[112] A. L. Patterson, *Physics Review*, 1934, **46**, 372–376.

[113] W. I. F. David, K. Shankland, N. Shankland, *Chemical Communications*, 1998, 931–932.

[114] F. Gozzo, B. Schmitt, T. Bortolamedi, C. Giannini, A. Guagliardi, M. Lange, D. Meister, D. Maden, P. Willmott, B. D. Patterson, *Journal of Alloys and Compounds*, 2004, **362**, 206–217.

[115] B. D. Patterson, R. Abela, H. Auderset, Q. Chen, F. Fauth, F. Gozzo, G. Ingold, H. Kuhne, M. Lange, D. Maden, D. Meister, P. Pattison, T. Schmidt, B. Schmitt, C. Schulze-Briese, M. Shi, M. Stampanoni, P. R. Willmott, *Nuclear Instruments Methods in Physics Research Section a-Accelerators Spectrometers Detectors and Associated Equipment*, 2005, **540**, 42–67.

[116] B. D. Patterson, C. Bronnimann, D. Maden, F. Gozzo, A. Groso, B. Schmitt, M. Stampanoni, P. R. Willmott, *Nuclear Instruments Methods in Physics Research Section B-Beam Interactions with Materials and Atoms*, 2005, **238**, 224–228.

[117] http://www.esrf.eu/UsersAndScience/Experiments/StructMaterials/ID31, *ESRF ID31*, 2010.

[118] L. de Broglie, *Annuals of Physics*, 1925, **3**, 22.

[119] P. C. H. Mitchell, S. F. Parker, A. J. Ramirez-Cuesta, TomkinsonJ., *World Scientific, Singapore*, 2005, Vibrational Spectroscopy with Neutrons With Applications in Chemistry, Biology, Materials Science and Catalysis.

[120] http://www.isis.stfc.ac.uk/about isis/aboutisis.html, *ISIS Homepage*, 2010.

[121] http://wwwisis2.isis.rl.ac.uk/disordered/gem.htm, *GEM home page*, 2010.

[122] A. C. Hannon, *Nuclear Instruments and Methods in Physics Research A*, 2005, **551**, 88.

[123] http://www.isis.stfc.ac.uk/instruments/hrpd/documents/hrpdmanual6735.pdf, *HRPD Manual*, 2010.

[124] http://www.isis.stfc.ac.uk/instruments/wish/, *WISH homepage*, 2010.

[125] A. Coelho, *TOPAS Academic*, 1992-2004.

[126] G. S. Pawley, *Journal of Applied Crystallography*, 1981, **14**, 357–361.

[127] W. I. F. David, K. Shankland, L. B. McCusker, C. Baerlocher, *Structure Determination from Powder Diffraction Data*, 2006, Oxford Science Publications.

[128] W. I. F. David, K. Shankland, J. van de Streek, E. Pidcock, W. D. S. Motherwell, J. C. Cole, *Journal of Applied Crystallography*, 2006, **39**, 910–915.

[129] H. M. Rietveld, *Journal of Applied Crystallography*, 1969, **2**, 65–, Part 2.

[130] M. O. Jones, P. P. Edwards, R. Lowton, M. Sommariva, W. I. F. David, *Preprints of Symposia - American Chemical Society, Division of Fuel Chemistry*, 2009, **54**, 687–688.

[131] E. S. W. Ridgefield, M. J. O'Neil, *Differential Microcalorimeter*, 1966, **U.S. Patent 3,263,484**.

[132] R. F. Speyer, *Thermal analysis of materials*, 1993, **CRC Press**.

[133] E. Pungor, *A Practical Guide to Instrumental Analysis*, Florida: Boca Raton., 1995.

[134] http://www.setaram.com/SENSYS-evo DSC.htm, *SENSYS-evo-DSC*, 2010.

[135] E. F. Kaufmann, *Characterisation of Materials*, 2003, **Wiley**, 343.

[136] P. Debye, *Annalen der Physik*, 1912, **344**, 789.

[137] http://www.qdusa.com/sitedocs/productBrochures/heatcapacity he3.pdf, $PPMS_QDUSA$, 2010.

[138] http://www.isis.stfc.ac.uk/instruments/tosca/, *TOSCA home page*, 2010.

[139] S. F. Parker, C. J. Carlile, T. Pike, J. Tomkinson, R. J. Newport, C. Andreani, F. P. Ricci, F. Sacchetti, M. Zoppi, *Physica B: Condensed Matter*, 1997, **241-243**, 154–156.

[140] D. Colognesi, M. Celli, F. Cilloco, R. J. Newport, S. F. Parker, V. Rossi-Albertini, F. Sacchetti, J. Tomkinson, M. Zoppi, *Applied Physics A: Materials Science Processing*, 2002, **74**, s64–s66.

[141] J. P. Perdew, K. Burke, M. Ernzerhof, *Physical Review Letters*, 1996, **77**, 3865.

[142] http://opium.sourceforge.net/sci.html., *Opium*, 2009.

[143] J. S. Lin, A. Qteish, M. C. Payne, V. Heine, *Physical Review B*, 1993, **47**, 4174.

[144] X. Gonze, *Physical Review B*, 1997, **55**, 10337.

[145] http://www.jmol.org/, *Jmol: an open-source Java viewer for chemical structures in 3D.*, 2009.

[146] A. J. Ramirez-Cuesta, *Computer Physics Communications*, 2004, **157**, 226–238.

[147] I. Bustinduy, F. J. Bermejo, T. G. Perring, G. Bordel, *Review of Scientific Instruments*, 2007, **78**, 043901.

[148] R. Coldea, *computer code MSLICE, a data analysis program for time-of-flight technique neutron spectrometers*, 2004.

[149] M. Levitt, *Spin Dynamics: Basics of Nuclear Magnetic Resonance*, 2001, John Wiley and Sons.

[150] M. D. Segall, P. J. D. Lindan, M. J. Probert, C. J. Pickard, P. J. Hasnip, S. J. Clark, M. C. Payne, *Journal of Physics: Condensed Matter*, 2002, **14**, 2717–2744.

[151] S. J. Clark, M. D. Segall, C. J. Pickard, P. J. Hasnip, M. J. Probert, K. Refson, M. C. Payne, *Zeitschrift fur Kristallographie*, 2005, **220**, 567–570.

[152] K. Refson, P. R. Tulip, S. J. Clark, *Physical Review B (Condensed Matter and Materials Physics)*, 2006, **73**, 155114–12.

[153] A. Jansen, M. Gerhards, *The Journal of Chemical Physics*, 2001, **115**, 5445.

[154] J. A. Salthouse, T. C. Waddington, *The Journal of Chemical Physics*, 1968, **48**, 5274–5275.

[155] http://www.tcm.phy.cam.ac.uk/castep/Phonons_Guide/CastepPhononsse6.html, *CASTEP manual*, 2006.

[156] H. Cho, W. J. Shaw, V. Parvanov, G. K. Schenter, A. Karkamkar, N. J. Hess, C. Mundy, S. Kathmann, J. Sears, A. S. Lipton, P. D. Ellis, S. T. Autrey, *Journal of Physical Chemistry A*, 2008, **112**, 4277–4283.

[157] N. J. Hess, M. R. Hartman, C. M. Brown, E. Mamontov, A. Karkamkar, D. J. Heldebrant, L. L. Daemen, T. Autrey, *Chemical Physics Letters*, 2008, **459**, 85–88.

[158] S. M. Kathmann, V. Parvanov, G. K. Schenter, A. C. Stowe, L. L. Daemen, M. Hartl, J. Linehan, N. J. Hess, A. Karkamkar, T. Autrey, *The Journal of Chemical Physics*, 2009, **130**, 024507.

[159] http://hyperphysics.phy astr.gsu.edu/hbase/mi.html, *hyperphysics*, 2010.

[160] W. A. Phillips, *Amorphous Solids: Low Temperature Properties*, 1981, Springer–Verlag, Berlin.

[161] T. S. Grigera, V. Martin-Mayor, G. Parisi, P. Verrocchio, *Nature*, 2009, **422**, 289.

[162] U. Buchenau, N. Nucker, A. J. Dianoux, *Phys. Rev. Lett.*, 1984, **53**, 2316–2319.

[163] F. Buchter, Z. Lodziana, P. Mauron, A. Remhof, O. Friedrichs, A. Borgschulte, A. Zuttel, D. Sheptyakov, T. Strassle, A. J. Ramirez-Cuesta, *Physical Review B*, 2008, **78**.

[164] A. I. Chumakov, I. Sergueev, U. van Bürck, W. Schirmacher, T. Asthalter, R. Rüffer, O. Leupold, W. Petry, *Phys. Rev. Lett.*, 2004, **92**, 245508.

[165] A. J. Ramirez-Cuesta, *Private communication*, June 2009.

[166] R. S. Seymour, A. W. Pryor, *Acta Crystallographica Section B-Structural Crystallography and Crystal Chemistry*, 1970, **B 26**, 1487–.

[167] R. Flacau, C. I. Ratcliffe, S. Desgreniers, Y. Yao, D. D. Klug, P. Pallister, I. L. Moudrakovski, J. A. Ripmeester, *Chem. Commun.*, 2010, **46**, 9164–9166.

[168] H. F. King, D. F. Hornig, *Journal of Chemical Physics*, 1966, **44**, 4520.

[169] W. I. F. David, *Fortan computer program - Fitter*.

[170] A. Einstein, *Annalen der Physik*, 1907, **22**, 180.

[171] W. I. F. David, R. M. Ibbertson, T. Matsuo, *Proc. R. Soc. Lond. A*, 1993, **442**, 129.

[172] A. G. Myers, B. H. Yang, H. Chen, J. L. Gleason, *Journal of the American Chemical Society*, 1994, **116**, 9361–9362.

[173] A. G. Myers, B. H. Yang, D. J. Kopecky, *Tetrahedron Letters*, **37**, 3623–3626, 19.

[174] A. Pross, L. Radom, *Tetrahedron*, 1980, **36**, 673–676.

[175] D. R. Armstrong, P. G. Perkins, G. T. Walker, *Journal of Molecular Structure: THEOCHEM*, 1985, **122**, 189–204.

[176] M. Ramzan, F. Silvearv, A. Blomqvist, R. H. Scheicher, S. Lebègue, R. Ahuja, *Phys. Rev. B*, 2009, **79**, 132102.

[177] R. A. Varin, T. Czujko, Z. S. Wronski, Z. Zaranski, *Canadian Metallurgical Quarterly*, 2009, **48**, 11–25.

[178] H. V. K. Diyabalange, R. P. Shrestha, T. A. Semelsberger, B. L. Scott, M. E. Bowden, A. K. Burrell, *Preprints of Symposia - American Chemical Society, Division of Fuel Chemistry*, 2008, **53**, 672.

[179] Z. Xiong, Y. Chua, G. Guotao Wu, W. Xu, P. Chen, W. Shaw, A. Karkamkar, J. Linehan, T. Smurthwaite, T. Autrey, *Chemical Communications*, 2008, **43**, 5595–5597.

[180] A. Luedtke, T. Autrey, *Inorganic Chemistry*, 2010, **49**, 3905–3910.

[181] H. V. K. Diyabalanage, A. K. Burrell, *Private communication*, July 2009.

[182] X. Yu, G. Xia, Y. Guo, L. Gao, *Faming Zhuanli Shenqing Gongkai Shuomingshu*, 2009, **2009-10049823**, 6pp–Patent CHINA.

[183] Z. Xiong, Y. Chua, G. Guotao Wu, L. Wang, M. Wong, Z. Kam, T. Autrey, T. Kemmitt, P. Chen, *Dalton Transactions*, 2010, **39**, 720–722.

[184] K. R. Graham, T. Kemmitt, M. E. Bowden, *Energy Environ. Sci.*, 2009, **2**, 706–710.

[185] D. Y. Kim, N. J. Singh, H. M. Lee, K. S. Kim, *Chemistry- A European Journal*, 2009, **15**, 5598–5604.

[186] T. B. Lee, M. L. McKee, *Inorganic Chemistry*, 2009, **48**, 7564–7575.

[187] S. Swinnen, V.-S. Nguyen, M.-T. Nguyen, *Chem. Phys. Lett.*, 2010, **489**, 148–153, Electrochemical, Radiational, and Thermal Energy Technology.

[188] V. Milman, B. Winkler, *Zeitschrift Fur Kristallographie*, 2001, **216**, 99–104.

[189] P. A. Chater, W. I. F. David, S. R. Johnson, P. P. Edwards, P. A. Anderson, *Chemical Communications*, 2006, 2439–2441.

[190] M. Lazzeri, A. Vittadini, A. Selloni, *Physical Review B*, 2001, **63**, 9.

[191] W. Miller, C. W. Smith, *Journal of Materials Science*, 2009, **44**, 5441–5451.

[192] G. Ernst, C. Broholm, G. R. Kowach, A. P. Ramirez, *Nature*, 1998, **396**, 147–149.

[193] G. Wolf, J. Baumann, F. Baitalow, F. P. Hoffmann, *Thermochimica Acta*, 2000, **343**, 19–25.

[194] W. Luo, R. Ahuja, Y. Ding, H. K. Mao, *Proceedings of the National Academy of Sciences of the United States of America*, 2007, **104**, 16428–16431.

[195] *CASTEP*, 2006, http://www.castep.org/CASTEP_talks_06/refson3.pdf.

[196] C. Gervais, F. Babonneau, *Journal of Organometallic Chemistry*, 2002, **657**, 75–82.

[197] S. Kroeker, J. F. Stebbins, *Inorganic Chemistry*, 2001, **40**, 6239.

[198] S. A. C. McDowell, T. S. Forde, *The Journal of Chemical Physics*, 2002, **117**, 6032–6037.

[199] http://wwwisis2.isis.rl.ac.uk/INSdatabase/Results.asp?Lithiumhydride, *TOSCA Database*, 2010.

[200] P. J. Fazen, E. E. Remsen, J. S. Beck, P. J. Carroll, A. R. McGhie, L. G. Sneddon, *Chemistry of Materials*, 1995, **7**, 1942–1956.

[201] G. Oszlányi, A. Süto, *Acta Crystallographica Section A*, 2008, **64**, 123–134.

[202] A. . Schlesinger, A. Burg, *Journal of the American Chemical Society*, 1938, **60**, 290 – 299.

[203] X. Yu, G. Xia, Y. Guo, L. Gao, *Faming Zhuanli Shenqing Gongkai Shuomingshu*, 2010, **CN 101746726**, 6pp–Patent CHINA.

[204] J. W. Moore, C. L. Stanitski, P. C. Jurs, *Chemistry: The Molecular Science*, Thomson Brooks/Cole, 2007.

[205] A. Zalkin, D. H. Templeton, *Journal of Physical Chemistry*, 1956, **60**, 821–823.

[206] Q. C. Ma, G. J. Zhang, Y. M. Kan, Y. B. Xia, P. L. Wang, *Ceramics International*, 2010, **36**, 167–171.

[207] M. Erdemoglu, *International Journal of Mineral Processing*, 2009, **92**, 144 – 152.

[208] G. Renaudin, S. Gomes, H. Hagemann, L. Keller, K. Yvon, *Journal of Alloys and Compounds*, 2004, **375**, 98–106.

[209] E. Gaffet, M. Harmelin, *Journal of the Less Common Metals*, 1990, **157**, 201.

[210] Y. Nakamori, K. Miwa, A. Ninomiya, H. Li, N. Ohba, S. Towata, A. Zttel, S. Orimo, *Phys. Rev. B*, 2006, **74**, 045126.

[211] U. B. Demirci, P. Miele, *Energy Environmental Science*, 2009, **2**, 627.

List of Tables

Appendix A

Inelastic Neutron Scattering Spectroscopy Modes and Assignments

Table A.1: Wavenumbers and assignments for the observed and calculated INS and Raman modes of α-$LiNH_2BH_3$ s, strong; m,medium; w, weak; sh, shoulder; br, broad; v, very.

INS cm^{-1}	DFT cm^{-1}	Raman cm^{-1}	DFT cm^{-1}	Assignment	Mulliken Labels
-	-0.08			Anharmonic accoustic translation	a
-	-0.07			Anharmonic accoustic translation	b
-	-0.05			Translation	c
39.00w	29.48			Translation	d
-	57.66			Anharmonic translation	e
77.00m	78.76			Anharmonic translation	f
80.00m	88.38			Lattice Libration	a
-	88.92			Lattice Libration	g
-	90.67			Lattice Libration	c
-	93.18			Lattice Libration	d
99.00s	94.42			Lattice Libration	f
113.00m	94.61			Lattice Libration	h
118.00m	117.76			Molecular Libration	e
123.00s	121.44			Molecular Libration	b
	127.05			Molecular Libration	a
-	127.55			Molecular Libration	g
136.00m	130.58			Lattice deformation	f
-	141.24			Lattice deformation	h
-	148.06			Lattice deformation	g
-	150.18			Lattice deformation	c
151.00sh	153.26			Lattice deformation	h
-	155.43			Lattice deformation	b
-	156.18			Lattice deformation	d
159.00s	158.95			Lattice deformation	g
	161.83			Lattice deformation	h
164.00s	165.42			Lattice deformation	e

INS cm^{-1}	DFT cm^{-1}	Raman cm^{-1}	DFT cm^{-1}	Assignment	Mulliken Labels
	173.77			Lattice deformation	c
-	175.08			Lattice deformation	d
181.00s	182.26			Lattice deformation	c
-	182.47			Lattice deformation	d
	186.78			Lattice deformation	b
-	186.81			Lattice deformation	e
	190.03			Lattice deformation	h
192.00s	191.69			Lattice deformation	g
198.00m	208.67			Lattice deformation	f
204.00m	210.08			Lattice deformation	a
211.00m	211.65			Lattice deformation	a
	217.08			Lattice deformation	f
	219.45			Lattice deformation	b
221.00sh	223.69			Lattice deformation	e
226.00m	227.40			Lattice deformation	c
231.00s	233.19	231.00br	232.00	Lattice deformation	d
-	236.80			Lattice deformation	h
243.00sh	237.57			Lattice deformation	g
247.00sh	240.60			Lattice deformation	d
250.00s	243.32			Lattice deformation	e
260.00s	243.51			Lattice deformation	b
270.00s	247.99			Lattice deformation	c
-	248.47			Lattice deformation	a
279.00s	275.02			Lattice deformation	f
	284.62			Lattice deformation	e
288.00sh	287.63			Lattice deformation	b
294.00m	297.08			Lattice deformation	h
302.00w	297.68			Lattice deformation	a
308.00w	300.80			Lattice deformation	g
315.00w	318.15			Lattice deformation	f

INS cm^{-1}	DFT cm^{-1}	Raman cm^{-1}	DFT cm^{-1}	Assignment	Mulliken Labels
340.00m	343.60			BH_3 Libration	b
347.00s	347.08			BH_3 Libration	e
362.00sh	368.70			BH_3 Libration	f
366.00sh	368.73			BH_3 Libration	g
	369.06			BH_3 Libration	a
373.00m	371.96			BH_3 Libration	h
398.00sh	397.27			BH_3 Libration	c
402.00w	397.74			BH_3 Libration	d
416.00w					
425.00w	429.48			NH_2 Libration	g
450.00sh	442.66			NH_2 Libration	h
451.00sh	447.81			NH_2 Libration	b
460.00s	458.73			NH_2 Libration	e
478.00s	474.81			NH_2 Libration	c
479.00s	476.19	463.00m	473.00	N-Li stretch	d
480.00s	480.92			NH_2 Libration	a
481.00s	483.64			NH_2 Libration	a
-	485.24			NH_2 Libration	c
489.00sh	488.06			NH_2 Libration	f
-	490.80			NH_2 Libration	g
494.00w	494.01			N-Li stretch	d
	496.17			N-Li stretch + NH_2 Libration	h
	496.18			NH_2 Libration	b
	499.65			N-Li stretch + NH_2 Libration	f
529.00w	511.01			N-Li stretch + NH_2 Libration	e
792.00sh	794.86			NH_2 Rocking	c
801.00m	797.76			NH_2 + BH_3 Rocking	a
808.00m	814.74			NH_2 + BH_3 Rocking	g
813.00m	815.22			NH_2 + BH_3 Rocking	b
818.00m	821.44			NH_2 + BH_3 Rocking	d
824.00m	823.03	820.00m	821.90	NH_2 + BH_3 Rocking	f

INS cm^{-1}	DFT cm^{-1}	Raman cm^{-1}	DFT cm^{-1}	Assignment	Mulliken Labels
825.00m	825.79			NH_2 + BH_3 Rocking	e
827.00sh	825.96			NH_2 + BH_3 Rocking	h
829.00sh	829.91			NH_2 + BH_3 Rocking	b
-	831.71			NH_2 + BH_3 Rocking	g
834.00sh	836.00			NH_2 + BH_3 Rocking	d
	838.04			NH_2 + BH_3 Rocking	c
	839.84			NH_2 + BH_3 Rocking	a
845.00s	842.74			NH_2 + BH_3 Rocking	f
	856.52			NH_2 + BH_3 Rocking	e
865.00s	858.63			NH_2 + BH_3 Rocking	h
874.00sh				NH_2 + BH_3 Rocking	
889.00w	893.72			B-N Stretch	d
889.00w	893.99			B-N Stretch	c
903.00sh	895.09	902.00m	895.80	B-N Stretch	b
914.00w	895.10			B-N Stretch	f
924.00w	895.23			B-N Stretch	a
942.00w	896.69			B-N Stretch	g
985.00w	897.94			NH_2 + BH_3 Rocking	e
-	898.86			NH_2 + BH_3 Rocking	h
1009.00sh	1013.36			NH_2 + BH_3 Rocking	a
	1014.18			NH_2 + BH_3 Rocking	c
1021.00s	1021.21			NH_2 + BH_3 Rocking	b
-	1023.91			NH_2 + BH_3 Rocking	d
-	1024.42			NH_2 + BH_3 Rocking	g
	1026.84	1028.00wbr	1022.00	NH_2 + BH_3 Rocking	f
1062.00w	1035.38			NH_2 + BH_3 Rocking	e
	1037.72			NH_2 + BH_3 Rocking	h
1110.00w	1122.30			NH_2 + BH_3 Rocking	h
-	1122.56			NH_2 + BH_3 Rocking	e
-	1125.04			NH_2 + BH_3 Rocking	b
-	1125.20			NH_2 + BH_3 Rocking	g

INS cm^{-1}	DFT cm^{-1}	Raman cm^{-1}	DFT cm^{-1}	Assignment	Mulliken Labels
1128.00w	1128.97			NH_2 + BH_3 Rocking	d
	1133.52	1131.00wbr	1128.90	NH_2 + BH_3 Rocking	c
1139.00br	1134.28			NH_2 + BH_3 Rocking	f
1143.00w	1138.44			B-N Stretch + BH_3 Rocking	a
1151.00br	1154.62			B-N Stretch + BH_3 Rocking	b
1153.00m	1155.28			B-N Stretch + BH_3 Rocking	g
1174.00sh	1155.68			B-N Stretch + BH_3 Rocking	a
1197.00m	1157.27			B-N Stretch + BH_3 Rocking	e
-	1157.66			B-N Stretch + BH_3 Rocking	h
-	1162.18			B-N Stretch + BH_3 Rocking	d
-	1164.03			B-N Stretch + BH_3 Rocking	c
-	1164.57	1167.00vbr	1158.90	B-N Stretch + BH_3 Rocking	f
-	1238.00			BH_3 Wagging	d
-	1238.46			BH_3 Wagging	c
-	1240.97			BH_3 Wagging	h
-	1241.09			BH_3 Wagging	g
-	1243.01			BH_3 Wagging	a
-	1243.78			BH_3 Wagging	f
-	1244.07			BH_3 Wagging	e
-	1244.11			BH_3 Wagging	b
-	1256.95			BH_3 Wagging	f
-	1257.79			BH_3 Wagging	a
-	1257.92			BH_3 Wagging	d
-	1258.10			BH_3 Wagging	h
1271.00s	1258.71			BH_3 Wagging	c
1284.00sh	1258.88			BH_3 Wagging	g
1405.00w	1261.32	1260.00m	1237.70	BH_3 Wagging	e
1462.00w	1262.01		1257.90	BH_3 Wagging	b
1538.00m	1563.13	1536.00w	1571.00	NH_2 Wagging	g
1559.00sh	1563.20			NH_2 Wagging	b
1566.00w	1568.04			NH_2 Wagging	e

INS cm^{-1}	DFT cm^{-1}	Raman cm^{-1}	DFT cm^{-1}	Assignment	Mulliken Labels
-	1568.10			NH_2 Wagging	h
-	1570.07			NH_2 Wagging	a
-	1574.49			NH_2 Wagging	d
-	1574.81			NH_2 Wagging	f
-	1577.78			NH_2 Wagging	c
-				NH_2 Wagging	
1615.00w				NH_2 Wagging	
1631.00w				NH_2 Wagging	
1715.00w				NH_2 Wagging	
1876.00w				Asymmetric B-H stretch	
2148.00b	2190.95	2152.00mbr	2190.10	Asymmetric B-H stretch	a
2160.00w	2191.41			Asymmetric B-H stretch	d
-	2192.77	2190.00mbr	2230.90	Asymmetric B-H stretch	f
	2197.51			Asymmetric B-H stretch	c
-	2199.14			Asymmetric B-H stretch	b
-	2199.97			Asymmetric B-H stretch	e
-	2200.37			Asymmetric B-H stretch	g
-	2200.72			Asymmetric B-H stretch	h
2202.00mb	2231.78			Asymmetric B-H stretch	d
2223.00sh	2232.48			Asymmetric B-H stretch	c
2223.00sh	2233.79			Asymmetric B-H stretch	h
	2234.73			Asymmetric B-H stretch	g
-	2239.28			Symmetric B-H stretch	a
-	2244.17			Symmetric B-H stretch	b
-	2244.32			Asymmetric B-H stretch	e
	2246.10			Asymmetric B-H stretch	f
-	2304.78			Asymmetric B-H stretch	g
-	2306.83	2252.00mbr	2310.00	Symmetric B-H stretch	h
2292.00m	2311.49			Asymmetric B-H stretch	c
-	2311.55			Asymmetric B-H stretch	d
-	2315.23			Asymmetric B-H stretch	a

INS cm^{-1}	DFT cm^{-1}	Raman cm^{-1}	DFT cm^{-1}	Assignment	Mulliken Labels
-	2321.64			Asymmetric B-H stretch	b
2316.00sh	2322.41			Asymmetric B-H stretch	e
2383.00w	2326.91	2372.00w		Asymmetric B-H stretch	f
-	3382.23			Asymmetric B-H stretch	f
	3382.30			Symmetric N-H stretch	d
3279.00w	3382.61		-	Symmetric N-H stretch	a
	3382.98	3303.00s	3381.90	Symmetric N-H stretch	c
-	3384.94			Symmetric N-H stretch	g
-	3384.97			Symmetric N-H stretch	b
-	3385.55			Symmetric N-H stretch	h
-	3385.63			Symmetric N-H stretch	e
-	3453.04			Asymmetric N-H stretch	b
	3453.08			Asymmetric N-H stretch	g
	3453.62			Asymmetric N-H stretch	h
	3453.95			Asymmetric N-H stretch	e
	3454.14			Asymmetric N-H stretch	f
	3454.23			Asymmetric N-H stretch	d
	3454.51			Asymmetric N-H stretch	a
3459.00w	3454.99			Asymmetric N-H stretch	c
3520.00w		3360.00s	3453.50	Asymmetric N-H stretch	

Table A.2: Wavenumbers and assignments for the observed and calculated INS and Raman modes of α-NH_2BH_3 s, strong; m,medium; w, weak; sh, shoulder; br, broad; v, very.

	Representation	Mul	E	2	2	2	I	m	m	m
a	$B3_u$	24	1	-1	-1	1	-1	1	1	-1
b	$B2_u$	24	1	-1	1	-1	-1	1	-1	1
c	$B1_u$	24	1	1	-1	-1	-1	-1	1	1
d	A_g	24	1	1	1	1	1	1	1	1
e	$B3_g$	24	1	-1	-1	1	1	-1	-1	1
f	$B2_g$	24	1	-1	1	-1	1	-1	1	-1
g	A_u	24	1	1	1	1	-1	-1	-1	-1
h	$B1_g$	24	1	1	-1	-1	1	1	-1	-1

Table A.3: Wavenumbers and assignments for the observed and calculated INS and Raman modes of KNH_2BH_3 s, strong; m,medium; w, weak; sh, shoulder; br, broad; v, very.

INS cm^{-1}	DFT cm^{-1}	Assignment
	-254.87	anharmonic lattice vibration
	-0.04	anharmonic lattice vibration
	-0.03	anharmonic lattice vibration
	-0.03	anharmonic lattice vibration
54.59	59.19	harmonic lattice vibration inner KAB2
58.01	64.24	harmonic lattice vibration inner KAB2
62.15	66.89	harmonic lattice vibration inner KAB2
68.32	68.33	harmonic lattice vibration inner KAB2
	69.18	harmonic lattice vibration inner KAB2
71.84	70.30	harmonic lattice vibration outer KAB2
75.12	81.57	harmonic lattice vibration outer KAB2
83	84.13	harmonic lattice vibration Ks along a direction
86.81	85.59	harmonic lattice vibration Ks along a direction
	87.76	harmonic lattice vibration Ks along a direction
	87.77	harmonic lattice vibration outer KABS
	89.62	harmonic lattice vibration
97.74	97.23	harmonic lattice vibration Ks along c direction
	97.65	harmonic lattice vibration K1s along c direction
	97.74	harmonic lattice vibration K1s along c direction
	97.93	harmonic lattice vibration
	98.08	harmonic lattice vibration K1s along c direction
	100.22	harmonic lattice vibration K1s along b direction
	101.01	harmonic lattice vibration Ks along c direction
	101.02	harmonic lattice vibration K2 along c direction
	105.16	harmonic lattice vibration K2 along c direction
	105.74	harmonic lattice vibration inner KAB2 along b
	105.86	harmonic lattice vibration K2 along c direction

INS cm^{-1}	DFT cm^{-1}	Assignment
105.97	105.90	harmonic lattice vibration K1s and AB2s along c direction
	108.83	harmonic lattice vibration Ks and AB2s along c direction
	109.12	harmonic lattice vibration Ks and AB2s along b direction
109.76	109.63	harmonic lattice vibration Ks and AB2s along b direction
	110.96	harmonic lattice vibration
	111.42	harmonic lattice vibration KAB1 along a
112.51	112.98	harmonic lattice vibration
	114.55	harmonic lattice vibration KAB1 along a
	114.73	harmonic lattice vibration KAB1 along b
	115.75	harmonic lattice vibration
	119.21	harmonic lattice vibration
121.25	121.06	harmonic lattice vibration Ks along b direction
	124.45	harmonic lattice vibration Ks along b direction
126.19	127.76	harmonic lattice vibration Ks along b direction
	129.25	harmonic lattice vibration Ks along b direction
129.37	129.54	harmonic lattice vibration
135.42	130.67	harmonic lattice vibration
	136.67	harmonic lattice vibration AB2 along a direction
138.04	138.37	harmonic lattice vibration AB2 along a direction
139.43	139.75	harmonic lattice vibration K2 along a direction
	140.34	harmonic lattice vibration K2 along a direction
142.23	144.17	harmonic lattice vibration
	150.64	harmonic lattice vibration
	151.86	harmonic lattice vibration KAB2 along a direction
153.28	152.63	harmonic lattice vibration KAB2 along a direction
	154.35	harmonic lattice vibration KAB2 along a direction
	159.55	harmonic lattice vibration KAB1 along b direction
	159.67	harmonic lattice vibration KAB2 along a direction
	163.92	harmonic lattice vibration KAB1 along b direction
	166.59	harmonic lattice vibration
169.36	168.11	harmonic lattice vibration KAB1 along b direction
173.64	173.33	harmonic lattice vibration KAB2 along b direction
105.97	105.90	harmonic lattice vibration K1s and AB2s along c direction

INS cm^{-1}	DFT cm^{-1}	Assignment
178.02	179.09	harmonic lattice vibration KAB2 along b direction
	180.37	harmonic lattice vibration KAB1 along b direction
	181.87	harmonic lattice vibration
	181.97	harmonic lattice vibration
	183.37	harmonic lattice vibration
	183.59	harmonic lattice vibration ABs along c
184.34	183.89	harmonic lattice vibration ABs along c
	185.14	harmonic lattice vibration
188.06	190.00	harmonic lattice vibration
189.89	190.88	harmonic lattice vibration K1s and AB2s along a direction
	190.96	harmonic lattice vibration
	191.01	harmonic lattice vibration
	194.43	harmonic lattice vibration ABs along c
	194.55	harmonic lattice vibration
195.71	195.15	harmonic lattice vibration
	196.23	harmonic lattice vibration
	196.61	harmonic lattice vibration
	199.01	harmonic lattice vibration ABs
	200.43	harmonic lattice vibration ABs
	202.09	harmonic lattice vibration ABs
	202.77	harmonic lattice vibration ABs
	203.32	harmonic lattice vibration ABs
	203.53	harmonic lattice vibration ABs
206.76	206.44	harmonic lattice vibration ABs
210.92	208.06	harmonic lattice vibration ABs
218.44	221.94	harmonic lattice vibration ABs
	222.87	harmonic lattice vibration ABs
223.93	223.43	harmonic lattice vibration ABs
227.3	227.14	harmonic lattice vibration ABs
	230.74	harmonic lattice vibration ABs
	230.82	harmonic lattice vibration ABs

INS cm^{-1}	DFT cm^{-1}	Assignment
	231.61	harmonic lattice vibration ABs
233.05	233.96	harmonic lattice vibration ABs
	235.89	harmonic lattice vibration ABs
	236.45	harmonic lattice vibration ABs
241.32	243.78	harmonic lattice vibration ABs
247.42	245.54	harmonic lattice vibration ABs
252.41	263.13	harmonic lattice vibration ABs
262.68	270.15	harmonic lattice vibration ABs
267.97	274.66	harmonic lattice vibration ABs
273.37	276.20	harmonic lattice vibration ABs
	276.31	harmonic lattice vibration ABs
	276.53	harmonic lattice vibration ABs
	277.16	harmonic lattice vibration ABs
	278.25	harmonic lattice vibration ABs
	283.30	harmonic lattice vibration ABs
	284.68	harmonic lattice vibration ABs
	285.27	harmonic lattice vibration ABs
	285.92	harmonic lattice vibration ABs
	287.91	harmonic lattice vibration ABs
	288.38	harmonic lattice vibration ABs
	290.47	harmonic lattice vibration ABs
291.68vwb	291.18	harmonic lattice vibration ABs
	293.66	harmonic lattice vibration ABs
	294.08	harmonic lattice vibration ABs
	296.20	harmonic lattice vibration ABs
	298.95	harmonic lattice vibration ABs
	300.44	harmonic lattice vibration ABs
	302.70	harmonic lattice vibration ABs
	302.87	harmonic lattice vibration ABs
	310.37	harmonic lattice vibration ABs
315.92vwb	314.44	harmonic lattice vibration ABs

INS cm^{-1}	DFT cm^{-1}	Assignment
	316.93	harmonic lattice vibration ABs
	317.62	harmonic lattice vibration ABs
	318.62	harmonic lattice vibration ABs
	320.29	harmonic lattice vibration ABs
	321.77	harmonic lattice vibration ABs
332.07w	326.12	harmonic lattice vibration ABs
338.62w	340.70	BH3 wagging 2
347.31m	390.79	BH3 wagging 2
354.16s	390.90	BH3 wagging 2
361.46m	392.57	BH3 wagging 2
	393.73	BH3 wagging 2
	394.99	BH3 wagging 2
	395.79	BH3 wagging 2
	396.57	BH3 wagging 2
	397.76	BH3 wagging 2
447.91s	448.65	NH2 wagging 1
	450.54	NH2 wagging 1
	453.74	NH2 wagging 1
	454.83	NH2 wagging 1
459.55s	455.62	NH2 wagging 1
466.14s	457.42	NH2 wagging 1
485.12s	471.02	NH2 wagging 1
494.89s	472.79	NH2 wagging 1
	521.16	BH3 wagging 1
	523.02	BH3 wagging 1
	523.90	BH3 wagging 1
536.012vwb	525.05	BH3 wagging 1
	525.08	BH3 wagging 1
	525.93	BH3 wagging 1
	526.02	BH3 wagging 1
	527.55	BH3 wagging 1

INS cm^{-1}	DFT cm^{-1}	Assignment
	630.08	NH2 wagging 2
	631.46	NH2 wagging 2
	633.74	NH2 wagging 2
	634.53	NH2 wagging 2
	637.03	NH2 wagging 2
638.24vwb	637.06	NH2 wagging 2
	637.47	NH2 wagging 2
	637.75	NH2 wagging 2
	663.73	NH2 rocking 1
	664.83	NH2 rocking 1
677.09vwb	678.76	NH2 rocking 1
	681.17	NH2 rocking 1
691.27vwb	691.50	NH2 rocking 1
	693.42	NH2 rocking 1
	696.76	NH2 rocking 1
705.85vwb	701.30	NH2 rocking 1
	750.28	NH2 rocking 2
752.43mb	752.50	NH2 rocking 2
	753.81	NH2 rocking 2
	754.11	NH2 rocking 2
	754.97	NH2 rocking 2
763.77w	763.71	NH2 rocking 2
	765.74	NH2 rocking 2
779.16w	766.24	NH2 rocking 2
	812.94	BN rocking 1
815.34m	815.53	BN rocking 1
	818.52	BN rocking 1
	818.61	BN rocking 1
827.22m	831.40	BN rocking 1
	833.58	BN rocking 1
835.51m	833.98	BN rocking 1

INS cm^{-1}	DFT cm^{-1}	Assignment
843.89m	834.18	BN rocking 1
	874.80	BN rocking 2
	875.82	BN rocking 2
	875.98	BN rocking 2
	876.01	BN rocking 2
	876.61	BN rocking 2
	877.21	BN rocking 2
	877.86	BN rocking 2
878.24wb	878.96	BN rocking 2
887.04w	887.95	harmonic lattice vibration ABs
900.42w	923.80	harmonic lattice vibration ABs
913.99w	924.62	harmonic lattice vibration AB 1
923.16wb	925.26	harmonic lattice vibration ABs
	925.41	harmonic lattice vibration ABs
	925.52	harmonic lattice vibration ABs
	925.70	harmonic lattice vibration ABs
	926.63	harmonic lattice vibration AB 1
	935.07	harmonic lattice vibration AB 2
	935.29	harmonic lattice vibration AB 2
	935.57	harmonic lattice vibration AB 2
	936.62	harmonic lattice vibration ABs
941.56wb	940.32	harmonic lattice vibration AB 2
	942.36	harmonic lattice vibration AB 2
	942.89	harmonic lattice vibration AB 2
951.20wb	950.40	harmonic lattice vibration ABs
	993.60	BH3 wagging 1
	994.03	BH3 wagging 1
989.92w	994.46	BH3 wagging 1
	997.44	BH3 wagging 1
	997.82	BH3 wagging 2
	998.01	BH3 wagging 2

INS cm^{-1}	DFT cm^{-1}	Assignment
	998.48	BH3 wagging 1
	998.92	BH3 wagging 2
	1001.00	BH3 wagging 2
	1001.34	BH3 wagging 2
	1001.49	BH3 wagging 2
	1001.55	BH3 wagging 2
1004.84w	1002.01	BH3 wagging 1
	1002.47	BH3 wagging 2
	1003.92	BH3 wagging 2
1019.99wb	1015.23	BH3 wagging 1 and 2
	1097.47	BN rocking 1 and 2
	1099.77	BN rocking 1 and 2
1104wb	1102.00	BN rocking 1 and 2
	1102.93	BN rocking 1 and 2
	1114.36	BN rocking 1 and 2
1115.78	1116.13	BN rocking 1 and 2
	1116.39	BN rocking 1 and 2
	1117.97	BN rocking 1 and 2
	1134.49	BN rocking 1 and 2
	1135.02	N -H wagging
1138.28w	1135.04	N -H wagging
	1139.01	N -H wagging
	1146.34	N -H wagging
	1146.58	N -H wagging
	1147.31	N -H wagging
1149.63w	1147.59	N -H wagging
	1157.39	B-H bend
	1157.48	B-H bend
	1157.56	B-H bend
	1157.92	B-H bend
	1160.83	B-H umbrella mode

INS cm^{-1}	DFT cm^{-1}	Assignment
	1161.08	B-H umbrella mode
1161.34vw	1161.16	B-H umbrella mode
	1162.05	B-H umbrella mode
	1166.01	B-H umbrella mode
	1167.75	B-H umbrella mode
	1168.22	B-H umbrella mode
	1170.40	B-H umbrella mode
	1171.31	B-H umbrella mode
	1171.80	B-H umbrella mode
1172.86vwb	1172.17	B-H umbrella mode
	1173.08	B-H umbrella mode
	1174.40	B-H umbrella mode
	1177.07	B-H umbrella mode
	1178.71	B-H umbrella mode
	1179.45	B-H umbrella mode
	1179.62	B-H umbrella mode
	1179.97	B-H umbrella mode
	1181.46	B-H umbrella mode
	1181.95	B-H umbrella mode
1184.61w	1184.31	B-H umbrella mode
	1185.10	B-H umbrella mode
	1185.11	B-H umbrella mode
	1185.51	B-H umbrella mode
	1187.21	B-H umbrella mode
	1188.26	B-H umbrella mode
	1188.37	B-H umbrella mode
1196.49w	1189.12	B-H umbrella mode
	1225.21	B-H wagging mode

INS cm^{-1}	DFT cm^{-1}	Assignment
	1225.24	B-H wagging mode
	1225.45	B-H wagging mode
	1225.79	B-H wagging mode
1226.73wb	1226.15	B-H wagging mode
	1226.75	B-H wagging mode
	1226.77	B-H wagging mode
	1227.01	B-H wagging mode
	1256.16	B-H wagging mode
1257.68wb	1258.55	B-H wagging mode
	1258.61	B-H wagging mode
	1258.65	B-H wagging mode
	1259.36	B-H wagging mode
	1259.83	B-H wagging mode
	1260.54	B-H wagging mode
	1261.01	B-H wagging mode
	1535.33	BN stretch
	1535.45	BN stretch
	1540.65	BN stretch
	1540.89	BN stretch
	1540.97	BN stretch
	1541.32	BN stretch
	1541.76	BN stretch
	1542.07	BN stretch
	1545.72	BN stretch
	1547.02	BN stretch
	1547.38	BN stretch
	1547.38	BN stretch
	1547.57	BN stretch
	1548.19	BN stretch
1558.51vwb	1548.68	BN stretch
	1549.65	BN stretch

INS cm^{-1}	DFT cm^{-1}	Assignment
	2139.04	B-H stretch 1
2117.72vwb	2140.70	B-H stretch 1 and 2
	2140.93	B-H stretch 1 and 2
	2141.23	B-H stretch 2
	2141.68	B-H stretch 2
	2142.44	B-H stretch 1 and 2
	2147.38	B-H stretch 1 and 2
	2147.40	B-H stretch 2
	2148.50	B-H stretch 1 and 2
	2149.41	B-H stretch 1 and 2
	2149.97	B-H stretch 1 and 2
	2151.76	B-H stretch 1
	2152.00	B-H stretch 2
	2152.54	B-H stretch 2
	2152.66	B-H stretch 1
2166.15wb	2169.05	B-H stretch 1 and 2
	2201.08	B-H stretch 2
	2201.35	B-H stretch 2
	2202.74	B-H stretch 2
	2205.55	B-H stretch 2
2209.71wb	2205.81	B-H stretch 2
	2206.55	B-H stretch 2
	2207.52	B-H stretch 2
	2207.57	B-H stretch 2
	2261.82	B-H stretch 1
	2263.69	B-H stretch 1
	2263.77	B-H stretch 1
2265.76vwb	2265.98	B-H stretch 1
	2266.50	B-H stretch 1
	2266.59	B-H stretch 1

INS cm^{-1}	DFT cm^{-1}	Assignment
	2269.43	B-H stretch 1
	2269.76	B-H stretch 1
	2273.64	B-H stretch 1
	2274.38	B-H stretch 1
	2274.50	B-H stretch 1
	2274.80	B-H stretch 1
	2275.29	B-H stretch 1
	2275.86	B-H stretch 1
	2276.22	B-H stretch 1
	2276.27	B-H stretch 1
	2277.82	B-H stretch 1
	2278.40	B-H stretch 1 and 2
	2279.12	B-H stretch 1 and 2
	2280.81	B-H stretch 1 and 2
	2284.44	B-H stretch 1 and 2
	2285.09	B-H stretch 1 and 2
	2285.13	B-H stretch 1 and 2
2288.22vwb	2285.28	B-H stretch 1 and 2
	3383.45	N-H stretch 2
	3383.73	N-H stretch 2
	3383.82	N-H stretch 2
	3386.41	N-H stretch 2
	3386.51	N-H stretch 2
3393.54vwb	3387.26	N-H stretch 2
	3387.30	N-H stretch 2
3478.24vwb	3387.31	N-H stretch 2
	3484.89	N-H stretch 1 and 2
	3485.43	N-H stretch 1 and 2
	3485.55	N-H stretch 1 and 2
	3485.77	N-H stretch 1 and 2
	3486.67	N-H stretch 1 and 2

INS cm^{-1}	DFT cm^{-1}	Assignment
	3486.94	N-H stretch 1 and 2
	3487.00	N-H stretch 1 and 2
	3487.61	N-H stretch 1 and 2
	3507.25	N-H stretch 1 and 2
	3507.73	N-H stretch 1 and 2
	3508.33	N-H stretch 1 and 2
	3508.55	N-H stretch 1 and 2
	3509.27	N-H stretch 1 and 2
3513.82vwb	3509.59	N-H stretch 1 and 2
	3509.70	N-H stretch 1 and 2
	3509.72	N-H stretch 1 and 2
	3608.41	N-H stretch 1
	3608.81	N-H stretch 1
3602.55	3609.15	N-H stretch 1
	3609.16	N-H stretch 1
	3609.34	N-H stretch 1
	3609.41	N-H stretch 1
	3609.57	N-H stretch 1
	3609.76	N-H stretch 1